

The impact of starbursts on element abundance ratios

James W. Johnson * and David H. Weinberg*Department of Astronomy, The Ohio State University, 140 W. 18th Avenue Columbus, OH 43210, USA*

Accepted 2020 August 4. Received 2020 August 4; in original form 2019 November 6

ABSTRACT

We investigate the impact of bursts in star formation on the predictions of one-zone chemical evolution models, adopting oxygen (O), iron (Fe), and strontium (Sr), as representative α , iron-peak, and s-process elements, respectively. To this end, we develop and make use of the Versatile Integrator for Chemical Evolution (VICE), a PYTHON package designed to handle flexible user-specified evolutionary parameters. Starbursts driven by a temporary boost of gas accretion rate create loops in [O/Fe]–[Fe/H] evolutionary tracks and a peak in the stellar [O/Fe] distribution at intermediate values. Bursts driven by a temporary boost of star formation efficiency have similar effects, and they also produce a population of α -deficient stars during the depressed star formation phase following the burst. This α -deficient population is more prominent if the outflow rate is tied to a time-averaged star formation rate (SFR) instead of the instantaneous SFR. Theoretical models of Sr production predict a strong metallicity dependence of supernova and asymptotic giant branch star yields, though comparison to data suggests an additional, nearly metallicity-independent source. Evolution of [Sr/Fe] and [Sr/O] during a starburst is complex because of this metallicity dependence and the multiple time-scales at play. Moderate amplitude (10–20 per cent) sinusoidal oscillations in SFR produce loops in [O/Fe]–[Fe/H] tracks and multiple peaks in [O/Fe] distributions, a potential source of intrinsic scatter in observed sequences. We investigate the impact of a factor ~ 2 enhancement of Galactic star formation ~ 2 Gyr ago, as suggested by some recent observations. VICE is publicly available at <http://pypi.org/project/vice/>.

Key words: methods: numerical – galaxies: abundances – galaxies: evolution – galaxies: star formation – galaxies: stellar content.

1 INTRODUCTION

The elemental abundances and abundance ratios of stars encode information about the history of galactic enrichment and about the stellar processes that produce the elements. The ratio of α -element abundances to the iron abundance is an especially important diagnostic, because the α -elements (e.g. O, Mg, and Si) are produced primarily by massive stars with short lifetimes, while Fe is also produced in substantial amounts by Type Ia supernovae (SNe Ia) that explode after a wide range of delay times. In simple chemical evolution models with smooth star formation histories, the track of $[\alpha/\text{Fe}]$ versus $[\text{Fe}/\text{H}]$ ¹ first follows a plateau that reflects the IMF²-averaged yield of core-collapse supernovae (CCSNe), then turns downward as SNe Ia begin to add Fe without associated α -elements. If the model has continuing gas accretion, then the $[\text{Fe}/\text{H}]$ and $[\alpha/\text{Fe}]$ ratios tend to approach an equilibrium in which the production of new elements is balanced by dilution from freshly accreted gas and by depletion of metals from new star formation or outflows (Larson 1972; Finlator & Davé 2008; Andrews et al. 2017, hereafter AWSJ17; Weinberg, Andrews & Freudenberg 2017, hereafter WAF17).

In this paper, we examine the impact of starbursts – sudden and temporary increases in the star formation rate (SFR) – which perturb chemical evolution by temporarily boosting the rate of CCSNe

relative to SNe Ia from earlier generations of stars. We adopt one-zone evolution models in which stars form from and enrich a fully mixed gas reservoir subject to accretion and outflow (see e.g. Schmidt 1959, 1963; Larson 1972; Tinsley 1980 for classical examples; WAF17, AWSJ17 for more recent work). Although idealized, one-zone models may be a reasonable approximation for the evolution of dwarf galaxies. The Milky Way can be modelled as an annular sequence of one-zone models (Matteucci & Franco 1989), which may be connected by processes such as the radial migration of stars (Schönrich & Binney 2009; Minchev et al. 2017) and radial gas flows (Lacey & Fall 1985; Bilitewski & Schönrich 2012).

The $[\alpha/\text{Fe}]$ – $[\text{Fe}/\text{H}]$ tracks observed in the inner Milky Way agree well with the predictions of a one-zone model in which the star-forming gas disc contracts vertically over a period of ~ 2 Gyr (Hayden et al. 2015; Freudenberg et al. 2017). In the solar neighborhood, stars with high and low vertical velocities trace distinct $[\alpha/\text{Fe}]$ – $[\text{Fe}/\text{H}]$ tracks known as the ‘high- α ’ and ‘low- α ’ sequences (Bensby, Feltzing & Lundström 2003; Hayden et al. 2015), a bimodality whose origin is still not fully understood. AWSJ17 and WAF17 systematically investigate the influence of model parameters on the $[\alpha/\text{Fe}]$ – $[\text{Fe}/\text{H}]$ tracks of one-zone models with smooth star formation histories, with particular attention to the role of outflows in regulating the equilibrium metallicity. In agreement with previous studies of the galaxy mass–metallicity relation (e.g. Dalcanton 2007; Finlator & Davé 2008; Peebles & Shankar 2011; Zahid et al. 2012), they find that achieving a solar metallicity interstellar medium (ISM) requires strong outflows, with a mass-loading factor $\eta \equiv \dot{M}_{\text{out}}/\dot{M}_* \approx 2.5$ for a Kroupa (2001) IMF where every star of mass 8–100 M_{\odot} explodes as a CCSN with the yields predicted by Chieffi & Limongi (2004, 2013).

* E-mail: giganano9@gmail.com

¹We follow conventional notation in which $[X/Y] \equiv \log_{10}(X/Y) - \log_{10}(X_{\odot}/Y_{\odot})$.

²IMF: initial mass function.

Gilmore & Wyse (1991) investigated the impact of a bursty star formation history on $[\text{O}/\text{Fe}]$ – $[\text{Fe}/\text{H}]$ tracks, focusing on application to the Large Magellanic Cloud. WAF17 investigated a model in which a sudden change of star formation efficiency (SFE) induces a starburst, causing an upward jump in $[\text{O}/\text{Fe}]$ followed by a return to equilibrium (see their fig. 9). In this paper, we study the impact of starbursts more systematically, showing the different forms of $[\text{O}/\text{Fe}]$ – $[\text{Fe}/\text{H}]$ tracks and stellar $[\text{O}/\text{Fe}]$ distributions for bursts induced by a sudden influx of gas, a boost in gas accretion rate, or an increase of SFE. We also investigate the connection between starbursts and winds, considering the possibility that outflows are tied to a time-averaged SFR instead of the instantaneous SFR that governs the rate of CCSN enrichment. In addition to O and Fe, we examine strontium (Sr) as a representative element that has both a CCSN contribution and an asymptotic giant branch (AGB) star contribution with a metallicity dependent yield.

To this end, we have developed a publicly available³ PYTHON package, the Versatile Integrator for Chemical Evolution (VICE), which solves the integro-differential equations of a one-zone chemical evolution model. Compared to flexCE (AWSJ17),⁴ VICE has a simpler methodology in that it works directly from user-specified IMF-averaged yields rather than drawing CCSNe stochastically from the IMF of massive stars. VICE focuses instead on versatility in specifying star formation histories, gas accretion histories, and star formation laws as arbitrary functions of time, and it will automatically compute yield tables from a variety of sources if requested (e.g. Woosley & Weaver 1995; Iwamoto et al. 1999; Chieffi & Limongi 2004; Karakas 2010; Cristallo et al. 2011; Seitzzahl et al. 2013; Limongi & Chieffi 2018, among others to be added in subsequent versions). With a backend written in C, VICE also achieves powerful computing speeds while maintaining this level of flexibility. We anticipate adding further capabilities to VICE in the future, including extensions to multizone models.

Our models in this paper are motivated primarily by considerations of dwarf galaxies, which often show evidence of bursty star formation histories (e.g. Weisz et al. 2011, 2014). However, even local variations in star formation induced by passage of gas through a spiral arm can induce some of these effects, damped mainly by the fact that such events typically convert only a small fraction of the available gas into stars (WAF17). In their hydrodynamic simulations of disc galaxy formation, Clarke et al. (2019) find that massive clumps in young gas-rich discs convert much of their gas into stars and therefore self-enrich, following tracks in $[\alpha/\text{Fe}]$ – $[\text{Fe}/\text{H}]$ space that resemble those of our efficiency-induced starburst models below. They propose that a superposition of such bursts is responsible for the high- α sequence observed in the Milky Way $[\alpha/\text{Fe}]$ – $[\text{Fe}/\text{H}]$ diagram. In addition to bursts, we investigate here the effect of slow sinusoidal variations in SFR, finding that these less dramatic variations could produce scatter in $[\alpha/\text{Fe}]$ at fixed $[\text{Fe}/\text{H}]$, at least along the low- α sequence.

2 METHODS: THE ONE-ZONE APPROXIMATION

2.1 The gas supply, star formation rate, and star formation efficiency

Under the one-zone approximation, the fundamental assumption is instantaneous mixing of newly released metals throughout the star-forming gas reservoir. In practice, the validity of this

approximation depends on the ratio of the mixing time-scale to the depletion time-scale, i.e. the average time required for an ISM fluid element to be either incorporated into a star or ejected in an outflow. For conditions in typical star-forming disc galaxies, characteristic depletion times are ~ 0.5 – 10 Gyr (see discussion of WAF17 based on observations of Leroy et al. 2008). Simulations of turbulent diffusion in discs imply that azimuthal mixing times are a fraction of an orbital period while radial mixing times can be much longer, so that ISM mixing will typically erase azimuthal abundance variations but not radial gradients (Petit et al. 2015; Krumholz & Ting 2018). In the dwarf galaxy regime, length-scales are shorter while characteristic turbulent velocities are comparable, so instantaneous mixing should be a good approximation azimuthally and may become an adequate approximation galaxy-wide. However, we are unaware of systematic studies of metal-mixing in the dwarf galaxy regime.

Under the one-zone approximation, the equations of galactic chemical evolution (GCE) reduce to a system of integro-differential equations of mass with time, which can be integrated numerically. Under this formalism, the time-derivative of the gas-supply is given by

$$\dot{M}_g = \dot{M}_{\text{in}} - \dot{M}_* - \dot{M}_{\text{out}} + \dot{M}_{\text{returned}} \quad (1a)$$

$$\approx \dot{M}_{\text{in}} - \dot{M}_*(1 + \eta - r_{\text{inst}}) \quad (1b)$$

$$= \dot{M}_{\text{in}} - M_g \tau_*^{-1} (1 + \eta - r_{\text{inst}}) \quad (1c)$$

where \dot{M}_{in} is the mass infall rate, \dot{M}_* is the SFR, \dot{M}_{out} is the mass outflow rate, and $\dot{M}_{\text{returned}}$ is the rate of recycling. The SFE time-scale is defined by $\tau_* = M_g/\dot{M}_*$, and the parameters η and r_{inst} are discussed further below. VICE allows the user to specify the initial gas supply $M_{g,0}$ and the inflow rate \dot{M}_{in} as a function of time, in which case the SFR follows from the star formation law $\dot{M}_* = M_g/\tau_*$. Alternatively, the user can specify the star formation history \dot{M}_* itself or the gas supply at all times $M_g(t)$, with the star formation law supplying the remaining quantity. In these cases, the infall rate is determined implicitly by solving equation (1a). The former approach is somewhat more common in chemical evolution modelling, reflecting the expectation that a galaxy’s star formation history is ultimately governed by the rate at which it accretes gas from the surrounding circumgalactic medium. However, a galaxy’s star formation history can be estimated observationally while its accretion history cannot, and for analytic solution it is often more convenient to specify $\dot{M}_*(t)$ rather than $\dot{M}_{\text{in}}(t)$ as shown by WAF17. For the calculations in this paper, we specify $\dot{M}_{\text{in}}(t)$ and allow the SFR to follow from the gas supply unless otherwise specified.

As a default value for the SFE time-scale we adopt $\tau_* = 2$ Gyr, the typical value found for molecular gas in a wide range of star-forming galaxies (Leroy et al. 2008). The observationally inferred τ_* is lower in some starbursting systems, as short as ~ 100 Myr; however, the details of this relation are subject to the ongoing debate about the CO-to-H₂ conversion factor (for details, see the review in Kennicutt & Evans 2012). Relative to the total gas supply, the SFE time-scale will be longer if much of the reservoir is in atomic form, roughly $\tau_* = (2 \text{ Gyr})(1 + M_{\text{HI}}/M_{\text{H}_2})$. VICE allows the user to specify τ_* as a function of time, simultaneously allowing it to vary with the gas supply according to the Kennicutt–Schmidt relation (Schmidt 1959, 1963; Kennicutt 1998). If one views the gas reservoir as representing an annulus of a disc, with gas surface density $\Sigma_g = M_g/A_{\text{ann}}$, then the classic non-linear Kennicutt–Schmidt law $\dot{\Sigma}_* \propto \Sigma_g^{1.5}$ implies $\tau_* \propto M_g^{-0.5}$. We adopt this form in some of our calculations below Table 1.

³<https://github.com/giganano/VICE.git>.

⁴<https://github.com/bretthandrews/flexce>.

Table 1. Galactic chemical evolution parameters and their fiducial/unperturbed values adopted in this paper (if applicable). For further details on each parameter, see VICE’s science documentation, available at https://vice-astro.readthedocs.io/en/latest/science_documentation/index.html.

Quantity	Description	Fiducial/Unperturbed value
M_g	Gas supply	$\sim 6 \times 10^9 M_\odot$
\dot{M}_*	SFR	$\sim 3 M_\odot \text{ yr}^{-1}$
\dot{M}_{in}	Infall rate	$\sim 9 M_\odot \text{ yr}^{-1}$
\dot{M}_{out}	Outflow rate	$\eta(\dot{M}_*)\tau_s$
$\dot{M}_{\text{returned}}$	Recycling rate	Continuous (see equation 2)
τ_*	SFE time-scale (M_g/\dot{M}_*)	2 Gyr
η	Mass-loading factor ($\dot{M}_{\text{out}}/\dot{M}_*$)	2.5
ξ_{enh}	Outflow enhancement factor ($Z_{\text{out}}/Z_{\text{ISM}}$)	1
\dot{M}_x^{CC}	Rate of enrichment from CCSNe	N/A
y_x^{CC}	IMF-integrated fractional yield from CCSNe	O: 0.015; Fe: 0.0012; Sr: 3.5×10^{-8}
\dot{M}_x^{Ia}	Rate of enrichment from SNe Ia	N/A
y_x^{Ia}	IMF-integrated fractional yield from SNe Ia	O: 0.0; Fe: 0.0017; Sr: 0.0
\dot{M}_x^{AGB}	Rate of enrichment from AGB stars	N/A
$r_x^{\text{AGB}}(m_{\text{to}} Z)$	Fraction yield from an AGB star of mass m_{to} and metallicity Z	Crivallo et al. (2011)
$r(t)$	Cumulative return fraction (CRF)	N/A
$h(t)$	Main-sequence mass fraction (MSMF)	N/A
Z_{ISM}	Total metallicity by mass of the ISM	N/A

2.2 The cumulative return fraction

The CRF $r(t)$ is the fraction of a stellar population’s mass formed at $t = 0$ that has been returned to the ISM by a time t through stellar winds or supernova explosions. In VICE, we calculate $r(t)$ approximately by assuming that all stars with initial mass $M > 8 M_\odot$ leave a remnant of $1.44 M_\odot$ while those less than $8 M_\odot$ leave remnants of mass $0.394 M_\odot + 0.109 M$ (Kalirai et al. 2008). In these calculations, the main-sequence turn-off mass at a time t following the formation of a stellar population is assumed to be $M_{\text{to}}/M_\odot \approx (t/10 \text{ Gyr})^{-1/3.5}$, the same form as adopted in WAF17. While this formula is less accurate for high M_{to} , the return time-scale for these stars is much shorter than other chemical evolution time-scales anyway, so the approximation is adequate.

VICE calculates the time-dependent return rate from all previous stellar generations as:

$$\dot{M}_{\text{returned}}(t) = \int_0^t \dot{M}_*(t-t')r'(t')dt'. \quad (2)$$

Alternatively, one can make the approximation that all mass (from AGB stars as well as CCSNe) is returned instantaneously, in which case:

$$\dot{M}_{\text{returned}} = r_{\text{inst}}\dot{M}_*. \quad (3)$$

For a Kroupa IMF, the CRF is $r(t) \approx 0.37, 0.40,$ and 0.45 after 1, 2, and 10 Gyr, and WAF17 shows that the difference between $[\alpha/\text{Fe}]$ – $[\text{Fe}/\text{H}]$ evolution with the time-dependent return of equation (2) and the instantaneous approximation with $r_{\text{inst}} = 0.4$ is very small. None the less, numerical implementation of equation (2) is neither difficult nor time-consuming, so we use continuous recycling throughout this paper. We note that equation (3) is not equivalent to the ‘instantaneous recycling approximation’ as that term is most frequently used, where it implies instantaneous return of *newly produced* elements as well as the mass and metals that stars are born with. The full instantaneous recycling approximation is accurate for pure-CCSN elements if the star formation history is smooth on time-scales of ~ 100 Myr, but it is not an accurate description of SN Ia enrichment. While our one-zone models assume instantaneous mixing, they *do not* assume instantaneous recycling for enrichment by SN Ia or AGB stars.

2.3 The mass loading factor

For the outflow mass loading factor η we adopt a default value of 2.5, the same as WAF17, with the result that our models approach approximately solar abundances at late times given our adopted CCSN and SN Ia yields. However, as noted in Section 1, we also consider the possibility that the outflow rate is not tied to the instantaneous SFR but to some time-averaged value. This introduces an additional parameter, the smoothing time-scale τ_s , defined such that

$$\begin{aligned} \dot{M}_{\text{out}} &= \eta\langle\dot{M}_*\rangle_{\tau_s} \\ &= \begin{cases} \frac{\eta}{\tau_s} \int_{t-\tau_s}^t \dot{M}_*(t')dt' & (t > \tau_s) \\ \frac{\eta}{t} \int_0^t \dot{M}_*(t')dt' & (0 \leq t \leq \tau_s). \end{cases} \end{aligned} \quad (4)$$

If galactic winds are driven primarily by massive star winds, radiation pressure, and CCSNe, then the effective smoothing time-scale is likely to be short ($\tau_s \sim 50$ Myr), and smoothing will have little impact on chemical evolution if the SFR is smooth on these time-scales. However, if SNe Ia play a central role in driving winds, then effective smoothing times as long as $\tau_s \sim 1$ Gyr are possible, altering the relative ejection of CCSNe and SNe Ia elements from a shorter duration starburst. Cosmic ray feedback could also produce an intermediate smoothing time, because the energy deposited by CCSNe can be temporarily stored in cosmic rays before building up sufficiently to drive a wind. While VICE allows the user to specify η as a function of time, we do not consider models with a time-varying η here.

2.4 CCSNe

Following WAF17, we implement in VICE the instantaneous explosion approximation to CCSNe. This is a good approximation, because the lifetimes of CCSN progenitors ($\lesssim 40$ Myr for the least massive ones) are much shorter than the relevant time-scales of GCE. In our models, a given yield of some element X is ejected simultaneously with the formation of a stellar population at all time-steps:

$$\dot{M}_x^{\text{CC}} = y_x^{\text{CC}}(Z)\dot{M}_*, \quad (5)$$

where y_x^{CC} is the fraction of the stellar population's *total* mass that is converted to the element x at a metallicity Z . The CCSN yield is

$$y_x^{\text{CC}} = \frac{\int_{m_{\text{SN}}}^u m_x \frac{dN}{dm} dm}{\int_l^u m \frac{dN}{dm} dm}, \quad (6)$$

where m_x is the mass of the element x ejected in the explosion of a star of initial mass m , and dN/dm is the assumed stellar IMF, for which we adopt the Kroupa (2001) form throughout this work. We also adopt $l = 0.08$ and $u = 100 M_\odot$ as the lower and upper mass limits of the IMF and $m_{\text{SN}} = 8 M_\odot$ as the minimum progenitor mass for a CCSN explosion. If some stars above m_{SN} implode to black holes instead of exploding as supernovae, they will have much lower (possibly zero) values of m_x (e.g. Sukhbold et al. 2016).

Upon request VICE will calculate y_x^{CC} for a given element and metallicity from literature tables. It also allows users to adopt any numerical value or user-constructed functions of Z to describe the yield for any element in its simulations. In practice, supernova nucleosynthesis studies determine the value of m_x for of order 10 values of m at a specified metallicity and rotational velocity. To compute the numerator of equation (6), VICE linearly interpolates m_x^5 values between the two surrounding m values in the available yield grid, or linearly extrapolates m_x values from the two highest m values in the grid if it does not extend to $100 M_\odot$.

We discuss our adopted O and Fe CCSN yields in Section 2.7. We base our choices on WAF17, but WAF17 did not investigate Sr enrichment, which we are interested in as a tracer of s-process nucleosynthesis in both CCSN and AGB stars. For this reason, we conduct a thorough investigation of CCSN Sr yields and the metallicity dependence thereof. We reserve this discussion to Section 4.1, which focuses on Sr nucleosynthesis.

2.5 The SN Ia delay-time distribution (DTD)

We define $R_{\text{Ia}}(t)$ to be the rate of SNe Ia per unit stellar mass formed at a time t following an episode of star formation. Following WAF17 (see Appendix A therein), we set:

$$M_x^{\text{Ia}} = y_x^{\text{Ia}} \langle \dot{M}_* \rangle_{\text{Ia}}, \quad (7)$$

where

$$y_x^{\text{Ia}} \equiv m_x^{\text{Ia}} \int_{t_D}^{t_{\text{max}}} R_{\text{Ia}}(t) dt = m_x^{\text{Ia}} \frac{N_{\text{Ia}}}{M_*} \quad (8)$$

is the fractional yield of some element x from all SNe Ia that would explode between the minimum delay time t_D and a specified maximum time t_{max} . Here, m_x^{Ia} is the average mass yield of the element x per SN Ia, M_* is the mass of the stellar population, and

$$\langle \dot{M}_* \rangle_{\text{Ia}} \equiv \frac{\int_0^t \dot{M}_*(t-t') R_{\text{Ia}}(t') dt'}{\int_{t_D}^{t_{\text{max}}} R_{\text{Ia}}(t') dt'} \quad (9)$$

is the time-averaged SFR weighted by the SNe Ia DTD. In implementation, VICE enforces $t_{\text{max}} = 15$ Gyr always, though provided one is consistent in equations (8) and (9), the result of equation (7) is independent of the choice of t_{max} . This formulation implicitly assumes that R_{Ia} and m_x^{Ia} are independent of the birth population's metallicity. As discussed further in Section 2.7 below, we adopt a

power-law DTD with $R_{\text{Ia}} \propto t^{-1.1}$ and a minimum time delay of $t_D = 150$ Myr. VICE allows the user to specify alternative forms for the DTD, including user-constructed functional forms.

2.6 AGB stars

For AGB enrichment, we implement in VICE an algorithm that tracks the mass rate of change of a single stellar population to determine the mass in dying stars at each time-step. The rate of mass enrichment of an element x from AGB stars is then given by

$$\dot{M}_x^{\text{AGB}} = - \int_0^t y_x^{\text{AGB}}(m_{\text{to}}(t-t'), Z_{\text{ISM}}(t')) \dot{M}_*(t') h(t-t') dt' \quad (10)$$

where y_x^{AGB} is the yield of a star of mass m and total metallicity Z , and h is the main-sequence mass fraction, defined to be the fraction of a stellar population's mass that is in the form of main-sequence stars at a time t following its formation. By definition, $h = 1$ at $t = 0$, and declines monotonically; hence, the minus sign in equation (10). h is fully described by the adopted stellar IMF and the mass-lifetime relation (see VICE's Science Documentation for further details).

2.7 Adopted nucleosynthetic yields

For CCSN yields of O and Fe, we adopt the same values as WAF17, $y_{\text{O}}^{\text{CC}} = 0.015$ and $y_{\text{Fe}}^{\text{CC}} = 0.0012$, independent of metallicity. The former is approximately the value computed from the yields of Chieffi & Limongi (2004) for solar metallicity stars assuming a Kroupa IMF in which all stars with $M = 8\text{--}100 M_\odot$ explode. CCSN iron yields are difficult to predict from first principles; our choice yields a plateau at $[\text{O}/\text{Fe}] \approx +0.45$, in reasonable agreement with observations. Although we investigate Sr as a representative example of an AGB element, it is also expected to have a CCSN contribution. In Section 4, we examine the impact of various assumptions of the form of $y_{\text{Sr}}^{\text{CC}}$, including one with no metallicity dependence, one that depends linearly on Z , another with a $y_{\text{Sr}}^{\text{CC}} \propto 1 - e^{-kZ}$ dependence, and one in which $y_{\text{Sr}}^{\text{CC}} = 0$ as a limiting case describing pure AGB enrichment.

For the SN Ia iron yield we adopt $y_{\text{Fe}}^{\text{Ia}} = 0.0017$, similar to the values used by Schönrich & Binney (2009), AWSJ17, and WAF17. This value is based on a normalization of the SNe Ia DTD that yields $N_{\text{Ia}}/M_* = \int_{t_D}^{t_{\text{max}}} R_{\text{Ia}}(t) dt = 2.2 \times 10^{-3} M_\odot^{-1}$, consistent with $(2 \pm 1) \times 10^{-3} M_\odot^{-1}$ from Maoz & Mannucci (2012), and $m_{\text{Fe}}^{\text{Ia}} = 0.78 M_\odot$ from the W70 explosion model of Iwamoto et al. (1999). Because this enrichment channel is negligible for O and Sr, we adopt $y_{\text{Sr}}^{\text{Ia}} = 0$ throughout this work. As noted in Section 2.5, we adopt a $t^{-1.1}$ power-law DTD, again motivated by Maoz & Mannucci (2012), with a minimum delay time of $t_D = 150$ Myr. In principle, t_D could be as short as the lifetime of the most massive stars that produce white dwarfs (roughly 40 Myr), but it is not clear empirically whether the $t^{-1.1}$ power law extends to such small t . As a rule of thumb, it is useful to remember that a t^{-1} power-law DTD would yield equal numbers of SNe Ia per logarithmic time interval (i.e. the same number between 0.1–1 and 1–10 Gyr). Thus 1 Gyr is the approximate characteristic time for half of the SN Ia iron to be produced. If t_D is as short as 0.05 Gyr, then about 20 per cent of SNe Ia explode between 0.05 and 0.15 Gyr, enough to noticeably shift the 'knee' of the $[\alpha/\text{Fe}]$ – $[\text{Fe}/\text{H}]$ tracks. For our default $t_D = 0.15$ Gyr, these tracks are nearly identical to those of an exponential DTD with the same normalization (see fig. 11 of WAF17).

Recently Maoz & Graur (2017) argued for a lower DTD normalization of $N_{\text{Ia}}/M_* = (1.3 \pm 0.1) \times 10^{-3} M_\odot^{-1}$ for a Kroupa IMF, based on comparisons of the cosmic star formation history and the redshift-dependent SN Ia rate derived from cosmological surveys. Adopting

⁵Linearly in m , not $\log m$.

this lower normalization would require us to adopt lower values of y_{O}^{CC} , $y_{\text{Fe}}^{\text{CC}}$, and η to reproduce the observed [O/Fe]–[Fe/H] tracks in the Milky Way, reducing each by roughly a factor of two. Such a change is physically plausible, because many of the high-mass stars with the highest oxygen yields may collapse to black holes instead of exploding as CCSNe (see discussion by, e.g. Pejcha & Thompson 2015; Sukhbold et al. 2016, and observational evidence of Gerke, Kochanek & Stanek 2015; Adams et al. 2017). These changes would not alter our qualitative conclusions below, but they would change the detailed form of evolutionary tracks and element ratio distributions. Brown et al. (2019) found that the local specific SN Ia rate scales strongly (and inversely) with galaxy stellar mass, and they argue that this dependence may imply a metallicity-dependent $R_{\text{Ia}}(t)$ in addition to a DTD that produces more SNe Ia at early times. Adopting a metallicity-dependent $y_{\text{Fe}}^{\text{Ia}}$ would have a larger qualitative impact on our models (though as a practical matter it would be straightforward to implement within VICE). We reserve a more thorough investigation of empirical constraints on elemental yields to future work.

The AGB yields of s-process elements depend strongly on both stellar mass and birth metallicity. It is therefore not feasible to specify single yield values or simple time-dependent functional forms. Instead, VICE implements a grid of fractional yields on a table of stellar mass and metallicity. At each time-step, and for each element, it then determines the appropriate yield y_x^{AGB} in equation (10) via bilinear interpolation between elements on the grid. The current version of VICE allows users to adopt either the Cristallo et al. (2011) or Karakas (2010) yield tables, and we adopt the former for calculations in this paper. A future version of VICE will likely include more yield tables as well as the capability to handle user-specifications on the AGB yields of each element. We provide further discussion of Sr yields in Section 4.

2.8 Illustrations

For smooth star formation histories, VICE yields [O/Fe]–[Fe/H] tracks similar to those of AWSJ17, WAF17, and Freudenburg et al. (2017), who present comparisons to data for Milky Way stellar populations. In this paper, we focus on the ways that starbursts and subtler perturbations to the star formation history influence abundance tracks and distributions, and we do not attempt to model or interpret current observational data. For illustrative purposes, we present in Appendix A a comparison of VICE predictions to the dwarf galaxy abundance data of Kirby et al. (2010), for which low characteristic metallicities require quite different parameter choices from the Milky Way.

3 FIDUCIAL STARBURST MODELS

We begin by defining a GCE model with nearly constant star formation, which we will then perturb in a variety of ways. Our fiducial no-burst model has an infall rate of $\dot{M}_{\text{in}} = 9.1 M_{\odot} \text{ yr}^{-1}$ onto a galaxy with an initial gas supply of $M_{\text{g}} = 6.0 \times 10^9 M_{\odot}$, an SFE time-scale of $\tau_* = 2$ Gyr, a mass-loading factor of $\eta = 2.5$, $\tau_s = 0$, and $\xi_{\text{enh}} = 1$ (i.e. $Z_{\text{out}} = Z_{\text{gas}}$) with continuous recycling. We also adopt a power-law SN Ia delay-time distribution (DTD) with $R_{\text{Ia}} \propto t^{-1.1}$ and minimum delay time of $t_{\text{D}} = 150$ Myr. In short, this is a model with a constant infall rate and (nearly) constant SFR with parameters that do not change with time. The analytic model of WAF17 accurately describes the [O/Fe] evolution of this numerical model. Although we adopt explicit numerical values for the initial gas mass and \dot{M}_{in} , the [Fe/H] and [O/Fe] evolution would be unchanged

if we multiplied both of these quantities by the same constant factor. As shown by WAF17, the characteristic time for the evolution of O or other CCSN elements in such a model is the depletion time $\tau_{\text{dep}} \equiv \tau_*/(1 + \eta - r_{\text{inst}})$, while for Fe the evolutionary time-scale depends on both τ_{dep} and the characteristic SN Ia time-scale $\tau_{\text{Ia}} \sim 1\text{--}2$ Gyr.

3.1 Gas-driven starbursts

Our simplest starburst model is one in which a large amount of gas with a specified metallicity is added to the galaxy in a short amount of time. Here, ‘large’ means that the added gas is significant compared to the current gas supply and ‘short’ is relative to the time-scales associated with GCE, in particular the depletion time τ_{dep} . In this paper, we adopt the simplest scenario in which the added gas has zero metallicity, but any value can be used in VICE.

The top row of Fig. 1 compares two gas-driven starburst models to our burstless scenario. These models have the same parameters as the burstless scenario with the exception of the infall rate. In these models, the infall rate assumes a value of $\dot{M}_{\text{in}} = 5000 M_{\odot} \text{ yr}^{-1}$ for one $\Delta t = 1$ Myr time-step, thereby adding $\dot{M}_{\text{in}} \Delta t = 5 \times 10^9 M_{\odot}$ of zero metallicity gas essentially instantaneously. Red and blue curves show models with gas added at $t = 2$ and 5 Gyr, respectively. In each case, the nearly doubled gas supply causes a near doubling of the SFR. This burst decays on a time-scale of ~ 1 Gyr as the excess gas is consumed by star formation and outflows.

The evolution of these models in [O/Fe] versus [Fe/H] exhibits a ‘jump-and-hook’ trajectory. Dilution by pristine gas causes an instantaneous jump to lower [Fe/H] at fixed [O/Fe]. The burst of star formation elevates the rate of CCSN enrichment to SN Ia enrichment, so the ISM evolves to higher [O/Fe] as the metallicity increases. Eventually the impact of the starburst dies away and the [O/Fe] evolution returns to that of the unperturbed model.

The top right panel shows the normalized distribution of [O/Fe] in these models. The unperturbed model has two peaks in this distribution, the first at [O/Fe] $\approx +0.45$ for stars formed early in the model galaxy’s evolution when SN Ia enrichment is still negligible, and the second at [O/Fe] $\approx +0.08$ produced when the system has reached equilibrium and is forming stars at constant [Fe/H] and [O/Fe]. For our adopted yields, a constant SFR model evolves to slightly super-solar [O/Fe], but a mildly declining SFR model would evolve to solar [O/Fe] (see WAF17, fig. 3). A declining SFR would also boost the equilibrium [Fe/H] to solar instead of mildly sub-solar for our adopted yields and η . We have chosen to focus on perturbations of a constant SFR model for simplicity, but we have checked that our qualitative conclusions hold if the underlying model has exponentially declining star formation with $\tau_{\text{sh}} \approx 6$ Gyr.

The starburst models produce a third peak in this distribution at intermediate values of [O/Fe]. The lower edge of this peak corresponds to the value of [O/Fe] at the start of the burst, and the upper edge corresponds to the value of [O/Fe] at the top of the hook seen in the middle panel. The peak arises both because the system spends extra time at these [O/Fe] values and because the SFR is elevated during this time. Although the jump-and-hook trajectories are similar for the two starburst models, the arc in [O/Fe] is flatter for the earlier burst, which corresponds to a narrower peak in [O/Fe]. This difference arises because at $t = 2$ Gyr the CCSN/SN Ia ratio of the unperturbed model is still elevated compared to its eventual equilibrium ratio, so the extra boost from the starburst has a smaller relative impact.

A gas rich merger or violent dynamical disturbance may induce a very rapid increase in a galaxy’s supply of star-forming gas. However, a temporary boost in a galaxy’s gas accretion rate can also induce

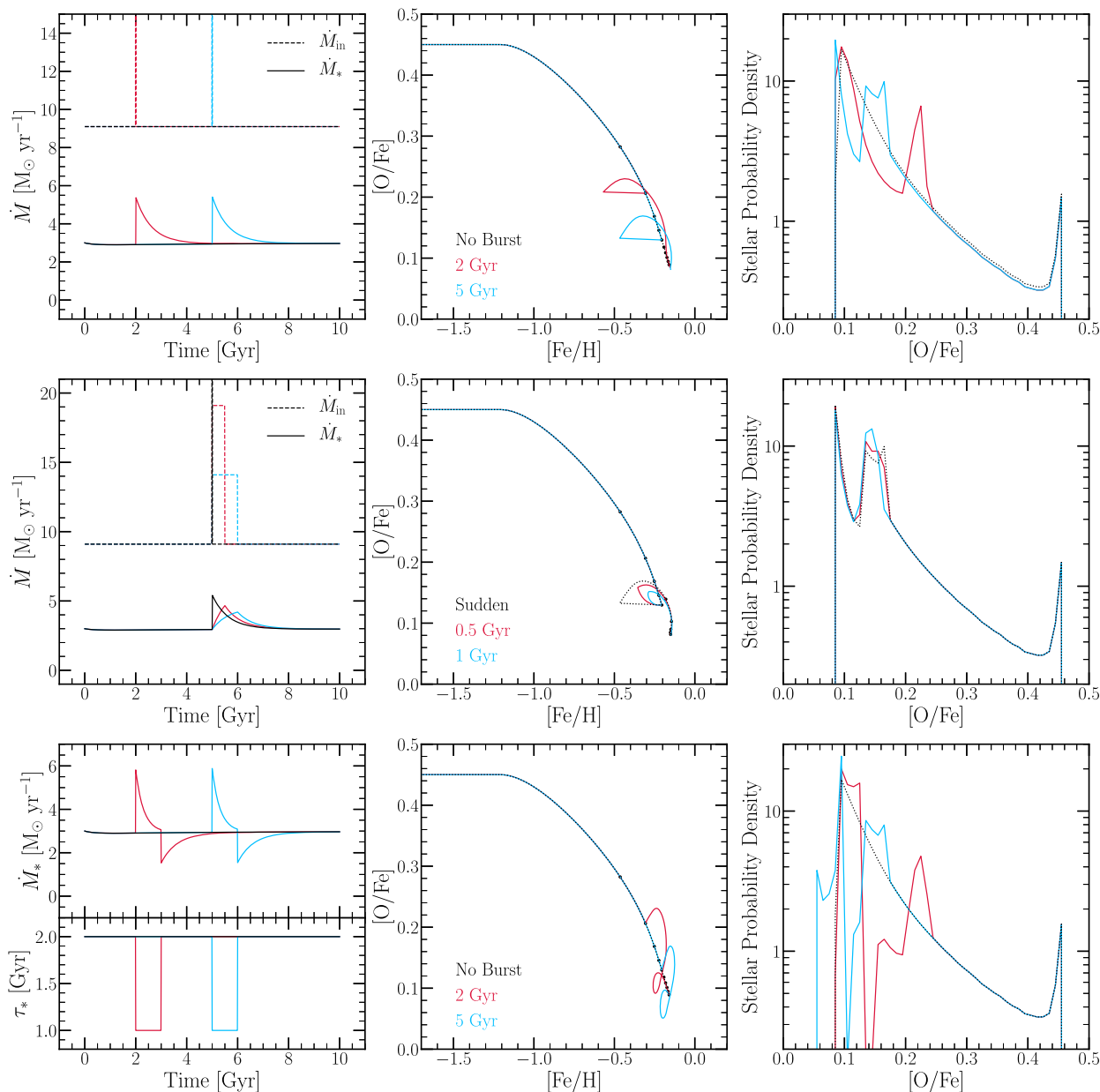


Figure 1. Evolutionary tracks in the $[O/Fe]$ – $[Fe/H]$ plane (middle column) and $[O/Fe]$ distributions (right column) of starburst GCE models with infall and star formation histories shown in left-hand panels. *Top:* Black curves show an unperturbed model with a constant infall rate and near-constant SFR. Red and blue curves show models with starbursts induced by adding 85 per cent of the ISM mass worth of $Z = 0$ gas at $t = 2$ or $t = 5$ Gyr, respectively. *Middle:* Red and blue curves show models in which the gas infall rate is boosted over a time interval of $\Delta t = 0.5$ or 1 Gyr, respectively, at $t = 5$ Gyr. Black curves show the sudden gas infall model from the upper row for comparison. The total amount of gas added is the same in all three models. *Bottom:* Red and blue curves show models with starbursts induced by doubling the SFE (halving τ_*) for an interval of $\Delta t = 1$ Gyr at $t = 2$ or 5 Gyr, respectively, with the infall rate (not plotted) held constant. Black curves show the unperturbed model. In the middle panels, small points on the unperturbed model curve mark 1 Gyr intervals.

elevated star formation. The middle row of Fig. 1 compares the $t = 5$ Gyr instantaneous gas increase model to models in which the same $5 \times 10^9 M_\odot$ of gas is added over $\Delta t = 0.5$ and 1.0 Gyr intervals. The perturbation to the SFR is smoother (left-hand panel), though the number of ‘extra’ stars formed is similar. The hooks in $[O/Fe]$ – $[Fe/H]$ are no longer flat-bottomed because the elevated SFR increases $[O/Fe]$ at the same time that the infall dilutes $[Fe/H]$. For $\Delta t = 1$ Gyr the jump in $[O/Fe]$ is small because the maximum boost of SFR is only about half that of the instantaneous model. However, the extra peak in the $[O/Fe]$ distribution is remarkably similar in all three

models, though slightly sharper for $\Delta t = 1$ Gyr. Although their model differs in detail, these findings are in good qualitative agreement with the ‘two-infall’ model predictions presented in Spitoni et al. (2019).

We conclude that a third peak in the $[O/Fe]$ distribution is the characteristic observable signature of a gas-driven starburst that formed a significant fraction of a system’s stars. The location of the peak indicates the value of $[O/Fe]$ at the time of the burst. Resolving these peaks requires a large sample of stars with precise $[O/Fe]$ (or $[\alpha/Fe]$) values, i.e. statistical errors of 0.05 dex or below. Correlating these $[\alpha/Fe]$ measurements with individual stellar age estimates

could increase the diagnostic power even if the age estimates have substantial statistical errors.

3.2 Efficiency-driven starbursts

The bottom row of Fig. 1 shows a scenario in which starbursts arise from a temporary increase of SFE instead of an increase in gas supply. We double the SFE – thus decreasing the SFE time-scale τ_* from 2 to 1 Gyr – for a period of $\Delta t = 1$ Gyr, beginning at $t = 2$ or 5 Gyr. The gas infall rate is held constant. As in the gas-doubling scenario, the SFR initially jumps by a factor of two, then decays to its original value. However, once τ_* returns to 2 Gyr, the SFR drops *below* that of the unperturbed model because the gas supply has been depleted during the high SFE phase. Over an interval of ~ 1 Gyr, the SFR recovers to the value of $\dot{M}_* \approx 3 M_\odot \text{ yr}^{-1}$ at which star formation and outflow balance infall.

The hooks in [O/Fe]–[Fe/H] evolution have a different morphology for the efficiency-driven bursts. Because there is no dilution by low-metallicity gas, the tracks jump up to higher [O/Fe] with slightly increasing [Fe/H], instead of first moving back to lower [Fe/H]. Furthermore, because of the depression in SFR once τ_* returns to its baseline value, the [O/Fe] track dips below that of the unperturbed model before returning to it at late times. During the downward loop, the rate of SNe Ia is high because of the stars formed during the recent burst, but the rate of CCSNe is low due to the reduced SFR.

The distribution of [O/Fe] in these models again shows an extra peak at [O/Fe] values close to those at the onset of the starburst. However, the morphology of these distributions is different from that of the gas-driven starburst models in two ways. First, the peak in [O/Fe] is followed by a much deeper trough at slightly lower [O/Fe] because the SFR is depressed while the ISM is evolving through this abundance ratio. Secondly, the [O/Fe] distribution acquires an additional peak at a value that corresponds to the bottom of the downward loops in the middle panel. With sufficiently good data, it might be possible to distinguish the signature of gas-driven and efficiency-driven starbursts from the detailed shape of the [O/Fe] distribution. In particular, an efficiency-driven burst at relatively late times would produce a population of roughly coeval stars with $[\alpha/\text{Fe}]$ values below that of the bulk population. There is some hint of such a population in the solar neighborhood (Feuillet et al. 2018).

3.3 Outflow smoothing time

We now examine models in which the outflow rate \dot{M}_{out} responds to the SFR averaged over a time interval τ_s instead of the instantaneous SFR. Fig. 2 shows star formation histories, [O/Fe]–[Fe/H] tracks, and [O/Fe] distributions for gas-driven and efficiency-driven starburst models with $\tau_s = 0, 0.5,$ and 1 Gyr. The $\tau_s = 0$ models are identical to the $t = 5$ Gyr burst models shown in the top and bottom rows of Fig. 1. Because the enhanced infall models (middle row of Fig. 1) are qualitatively similar to the instantaneous gas doubling model (top row), we show only this limiting case of a gas-driven starburst in the remainder of the paper.

For the gas-driven starburst, even a 1 Gyr smoothing time has only a small impact on the [O/Fe]–[Fe/H] trajectory and [O/Fe] distribution. Just after the accretion event, the SFR in the smoothed models is slightly higher than in the $\tau_s = 0$ model because the outflow rate is lower, and the hook in the evolutionary track therefore reaches slightly higher [O/Fe]. For $\tau_s = 1$ Gyr, the SFR at $t \approx 6\text{--}8$ Gyr dips below the $3 M_\odot \text{ yr}^{-1}$ baseline, because the extra accreted gas has been consumed and the outflow rate remains high because of the

earlier starburst. As a result, the deficit in the [O/Fe] distribution at $[\text{O}/\text{Fe}] \approx +0.1$ is deeper in this model.

For the efficiency-driven starburst, smoothing has a larger impact because the delayed outflow deepens the depression of SFR after the burst. The downward hook of [O/Fe] is therefore substantially deeper even for $\tau_s = 0.5$ Gyr. Smoothing of the outflow response exaggerates the characteristic form of an efficiency-driven starburst perturbation and moves the extra peak of the [O/Fe] distribution to a lower value.

3.4 Hybrid starbursts

If the gas supply of a galaxy increases suddenly, then the SFE may also increase because of greater gas self-gravity, more rapid cloud collisions, or whatever dynamical disturbance drove the gas increase in the first place. Observations provide some evidence for starbursts that are driven by both increased gas supply and increased SFE (Kennicutt & Evans 2012, and the citations therein). Fig. 3 shows results for a hybrid model in which a doubling of the gas supply is linked to a Kennicutt–Schmidt scaling of the SFE, with $\tau_* = (2 \text{ Gyr})(M_g/6 \times 10^9 M_\odot)^{-1/2}$ (see Section 2). If the smoothing time $\tau_s = 0$, then the evolution of this hybrid model is only slightly different from that of our standard gas-driven starburst, as one can see by comparing the dashed black and solid red curves in the middle and right-hand panels of Fig. 3. The hybrid burst has a higher peak SFR, which leads to a higher peak of the [O/Fe] hook. For $\tau_s = 1$ Gyr, the trajectory and [O/Fe] distribution of the hybrid model show features of both the gas-driven and efficiency-driven models. In particular, this model has a period of depressed SFR because of the delayed ejection of gas by the starburst, and the enhanced ratio of SNe Ia/CCSNe during this period causes a downward hook in [O/Fe] and an additional peak in the [O/Fe] distribution.

4 STRONTIUM

4.1 Nucleosynthesis

Strontium is one of the commonly used tracers of s-process nucleosynthesis in AGB stars (e.g. Conroy, van Dokkum & Graves 2013; Mishenina et al. 2019). Sr production differs from that of O and Fe, the two elements that we have examined thus far, because the delay time of AGB enrichment differs from that of SNe Ia and because the Sr yields of both CCSNe and AGB stars are expected to depend strongly on metallicity. Both of these differences have an important impact on predicted evolutionary tracks and element ratio distributions.

Fig. 4 plots IMF-averaged net CCSN yields of strontium based on the models of Chieffi & Limongi (2004) and Limongi & Chieffi (2018). These are the solutions to equation (6) with the same IMF parameters discussed in Section 2.4.

Chieffi & Limongi (2004) report Sr yields for non-rotating CCSN progenitors ($v_{\text{rot}} = 0$) at a wide range of metallicities, while Chieffi & Limongi (2013) report yields for $v_{\text{rot}} = 0$ and 300 km s^{-1} but at only solar metallicity. Progenitor rotation affects Sr yields from CCSNe due to rotationally induced mixing (Frischknecht et al. 2016). We presume the results of Chieffi & Limongi (2013) to be superseded by those of Limongi & Chieffi (2018), who examined a range of metallicities and values of $v_{\text{rot}} = 0, 150 \text{ km s}^{-1},$ and 300 km s^{-1} . However, we caution that the impact of rotation on the Sr yields at solar metallicity is much stronger in the Limongi & Chieffi (2018) study than in Chieffi & Limongi (2013) due to a different calibration of the rotation-induced mixing efficiency.

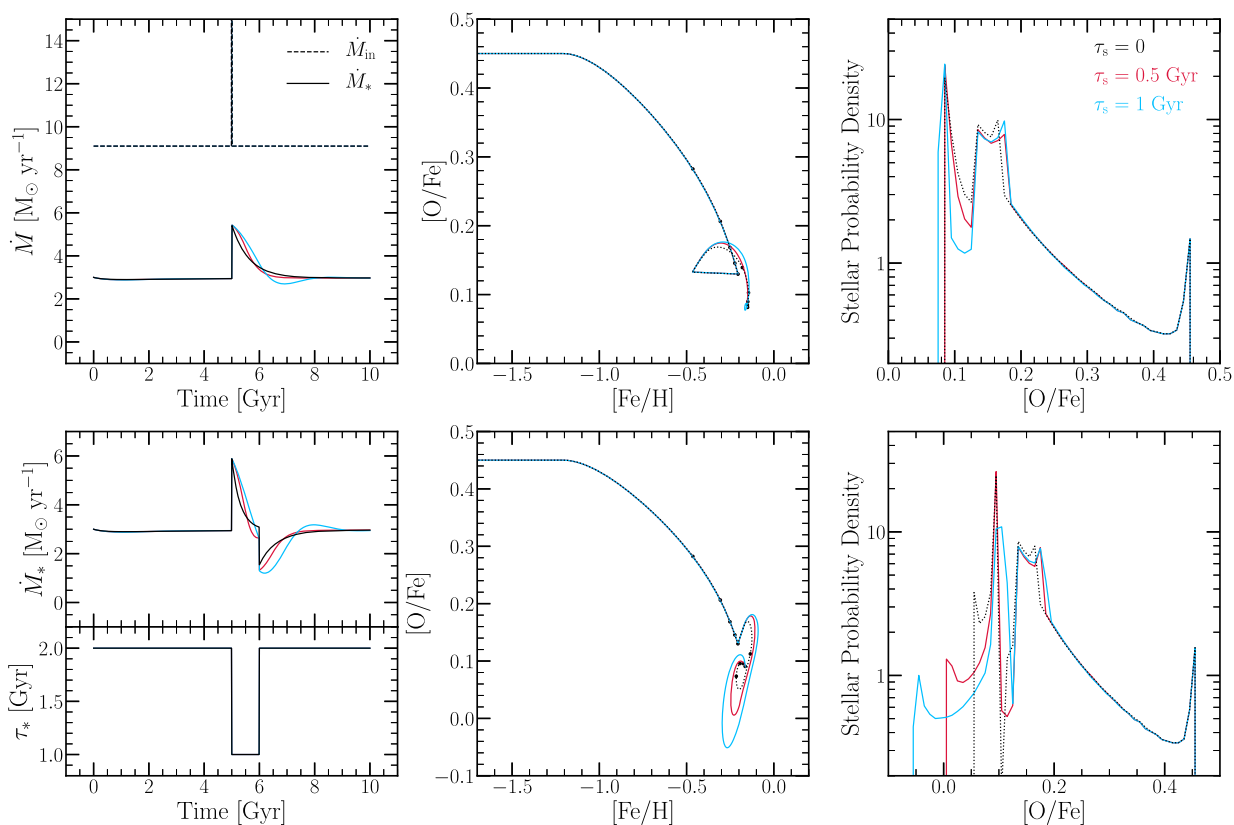


Figure 2. Similar to Fig. 1, for models in which the outflow $\dot{M}_{\text{out}} = \eta \langle \dot{M}_* \rangle_{\tau_s}$ responds to the SFR averaged over a preceding interval $\tau_s = 0.5$ (red) or 1 Gyr (blue). Top and bottom rows show models in which the starburst is induced by increasing the gas supply or SFE, respectively, at $t = 5$ Gyr, as in the top and bottom rows of Fig. 1. Black dotted curves show the corresponding $\tau_s = 0$ models, repeated from Fig. 1, with small dots at 1 Gyr intervals in the middle panels.

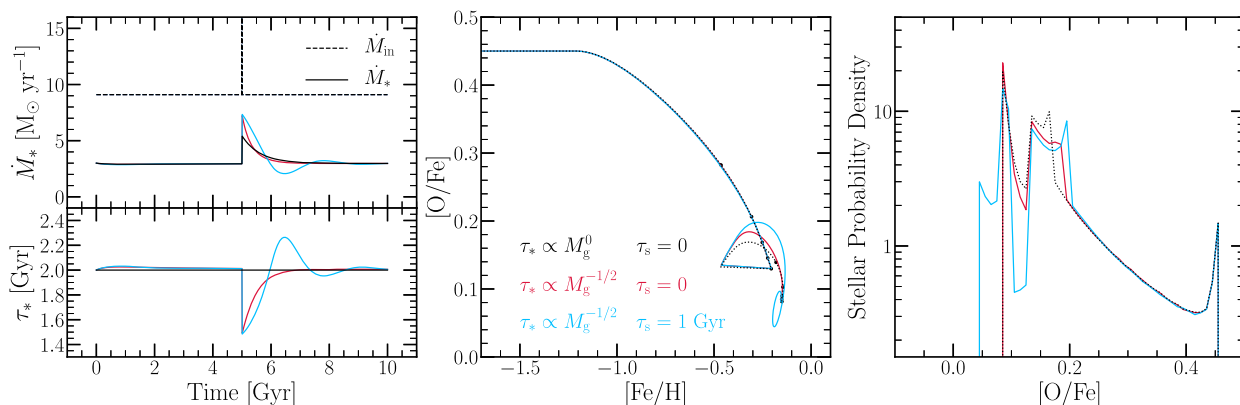


Figure 3. Similar to Fig. 1, for models in which the gas supply increases suddenly at $t = 5$ Gyr and the SFE time-scale remains constant (black dotted) or decreases in accordance with the Kennicutt–Schmidt law (red, blue). The blue curve model has smoothing time-scale $\tau_s = 1$ Gyr, and the black curve model is identical to the $t = 5$ Gyr starburst in the top row of Fig. 1. The lower left panel shows the response of τ_* to the evolving gas supply.

Fig. 4 shows that the predicted CCSN yields depend strongly on metallicity and are much higher (typically 1–3 orders of magnitude) for rapidly rotating versus non-rotating progenitors. As approximate descriptions of the numerical results, we show the functions

$$y_{\text{Sr}}^{\text{CC}} = 3.5 \times 10^{-8} (Z/Z_\odot) \quad (11a)$$

for $v_{\text{rot}} = 0$ and

$$y_{\text{Sr}}^{\text{CC}} = 10^{-7} [1 - e^{-10(Z/Z_\odot)}] \quad (11b)$$

for $v_{\text{rot}} = 150 \text{ km s}^{-1}$. For comparison, we will also compute GCE models with a constant $y_{\text{Sr}}^{\text{CC}} = 3.5 \times 10^{-8}$ matched to our linear model at $Z = Z_\odot$ and with $y_{\text{Sr}}^{\text{CC}} = 0$ corresponding to pure AGB enrichment. We caution that these are not fits to the yields plotted in Fig. 4; we adopt them as an agnostic approach to the form of the metallicity-dependent yield in the interval $-2 \lesssim [\text{Fe}/\text{H}] \lesssim 0$ in which our models are focused.

For AGB production of Sr, we use fractional yields as a function of initial stellar mass at various metallicities from the FRANEC code (Cristallo et al. 2011). These are plotted in the left-hand panel

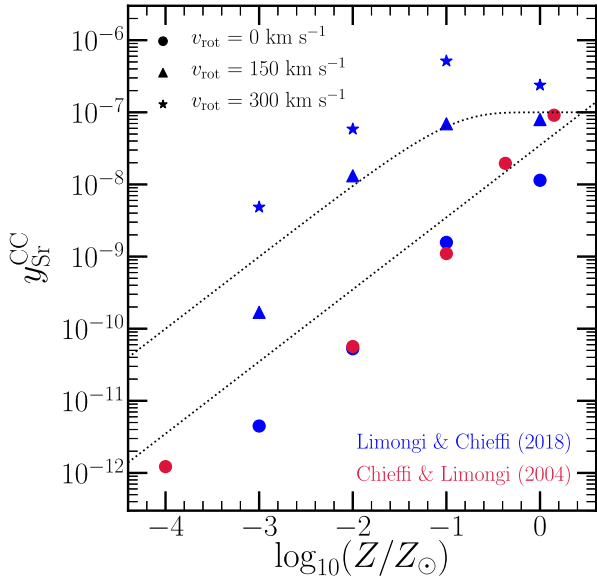


Figure 4. IMF-averaged CCSN yields of Sr computed using the non-rotating progenitor models of Chieffi & Limongi (2004), (red circles) and the models of Limongi & Chieffi (2018) for progenitors with $v_{\text{rot}} = 0$ (blue circles), 150 km s^{-1} (blue triangles), and 300 km s^{-1} (blue stars). Dotted curves show approximate characterizations of these results used in our GCE models, $y_{\text{Sr}}^{\text{CC}} = 3.5 \times 10^{-8} (Z/Z_{\odot})$ and $y_{\text{Sr}}^{\text{CC}} = 10^{-7} (1 - \exp(-10Z/Z_{\odot}))$. We adopt $Z_{\odot} = 0.014$ based on Asplund et al. (2009).

of Fig. 5, and they show two notable features. First, for near-solar metallicity the fractional yields are sharply peaked at stellar masses of $2\text{--}3 M_{\odot}$. To obtain the total mass yield per star one multiplies by M , giving weight to the contribution of higher mass stars, but the number of stars per linear ΔM interval is proportional to $M^{-2.3}$ for a Kroupa IMF in this mass range, thus increasing the weight of lower mass stars. The strong mass dependence of the fractional yields means that the IMF-averaged AGB yield is dominated by stars with relatively short lifetimes. The second notable feature is a strong metallicity

dependence, expected because the amount of Sr produced via the s-process during the AGB phase should increase with the abundance of free neutrons produced by nuclear reactions involving C and Ne isotopes. For $Z \lesssim Z_{\odot}/3$ the predicted fractional yields are below 10^{-7} at all masses, and for $Z \gtrsim Z_{\odot}/3$ the maximum fractional yield is roughly proportional to Z .

In the middle panel of Fig. 5, the black curve shows the late-time ($t = 10 \text{ Gyr}$), IMF-averaged AGB Sr yield as a function of metallicity. At $Z = Z_{\odot}$, the yield is $y_{\text{Sr}}^{\text{AGB}} = 5 \times 10^{-8}$, but for $Z < Z_{\odot}/3$ the yield is well below 10^{-8} . The green curve shows the total yield from adding $y_{\text{Sr}}^{\text{AGB}}$ to the $y_{\text{Sr}}^{\text{CC}}$ of equation (11a), which approximates the non-rotating Limongi & Chieffi (2018) models. At all metallicities for which $y_{\text{Sr}} > 10^{-8}$, the CCSN and AGB contributions are comparably important. However, for the $v_{\text{rot}} = 150 \text{ km s}^{-1}$ yields approximated by equation (11b), the CCSN yields dominate over the AGB yields at all metallicities (blue curve). The red curve shows the simple case of adding $y_{\text{Sr}}^{\text{AGB}}$ to a constant $y_{\text{Sr}}^{\text{CC}} = 3.5 \times 10^{-8}$.

The right-hand panel of Fig. 5 shows the time evolution of Sr production for a selection of metallicity values shown in the left-hand panel, $Z = 0.001, 0.003, 0.008,$ and 0.014 . All curves are normalized by the late-time yield, which is strongly dependent on metallicity as shown in the middle panel. Here, we adopt the $y_{\text{Sr}}^{\text{CC}} \propto Z$ yield model for CCSNe, and in all cases this accounts for about 40–50 per cent of the total yield. Typically about half of the AGB contribution comes within the first 0.5 Gyr, and nearly all of it within 2 Gyr. Dotted and dashed curves show the evolution of Fe production for our fiducial values of $y_{\text{Fe}}^{\text{CC}} = 0.0012$ and $y_{\text{Fe}}^{\text{Ia}} = 0.0017$ and a $t^{-1.1}$ DTD or an $e^{-t/1.5 \text{ Gyr}}$ DTD, respectively. Although our assumed minimum delay is $t_{\text{D}} = 0.15 \text{ Gyr}$, getting half of the SN Ia Fe contribution takes $\sim 0.9\text{--}1 \text{ Gyr}$, so the AGB Sr enrichment is faster, albeit moderately, than the SN Ia Fe enrichment. This rapid AGB contribution is a consequence of the dominant contribution from 2 to $4 M_{\odot}$ stars, which have short lifetimes. These curves represent the Sr production from a single population of stars at a given metallicity. In a GCE model, the metallicity itself rises with time, thus increasing the Sr production because of the metallicity-dependent yield. In the next section, we demonstrate that this complicates the enrichment time-scale of Sr relative to Fe.

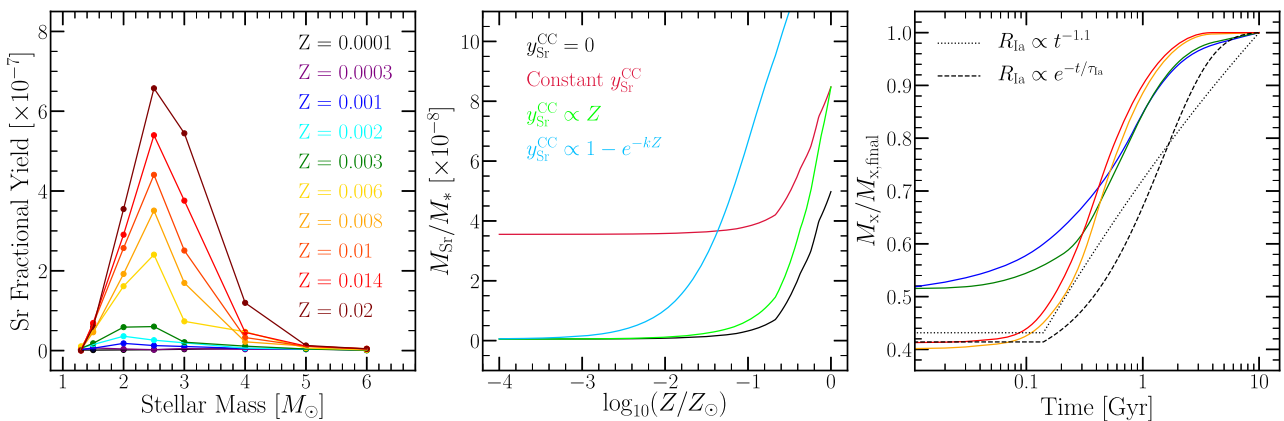


Figure 5. Yields of Sr as a function of stellar mass, metallicity, and time. *Left:* Fractional yields of AGB stars – the ejected Sr mass divided by the initial stellar mass, computed as a function of stellar mass and metallicity using the FRANEC code (Cristallo et al. 2011). *Middle:* IMF-averaged Sr yield after 10 Gyr, for a single stellar population of metallicity Z formed at $t = 0$, computed by adding the AGB yields to CCSN yields illustrated by the dotted curves in Fig. 4, or to constant yields $y_{\text{Sr}}^{\text{CC}} = 3.5 \times 10^{-8}$ or $y_{\text{Sr}}^{\text{CC}} = 0$ (AGB only). *Right:* Time evolution of Sr production for single stellar populations of metallicity $Z = 0.001, 0.003, 0.008,$ and 0.014 , assuming the $y_{\text{Sr}}^{\text{CC}} \propto Z$ model. Curves are colour coded to the legend in the left-hand panel. All curves are normalized to the final Sr mass produced after 10 Gyr, which depends strongly on Z as shown in the middle panel. Dotted and dashed black curves show the time evolution of Fe for our standard values of $y_{\text{Fe}}^{\text{CC}}$ and $y_{\text{Fe}}^{\text{Ia}}$ and a $t^{-1.1}$ or $e^{-t/1.5 \text{ Gyr}}$ DTD with a minimum delay time of 0.15 Gyr. Because AGB production is dominated by $2\text{--}4 M_{\odot}$ stars, AGB Sr enrichment from a single stellar population occurs faster than SN Ia Fe enrichment.

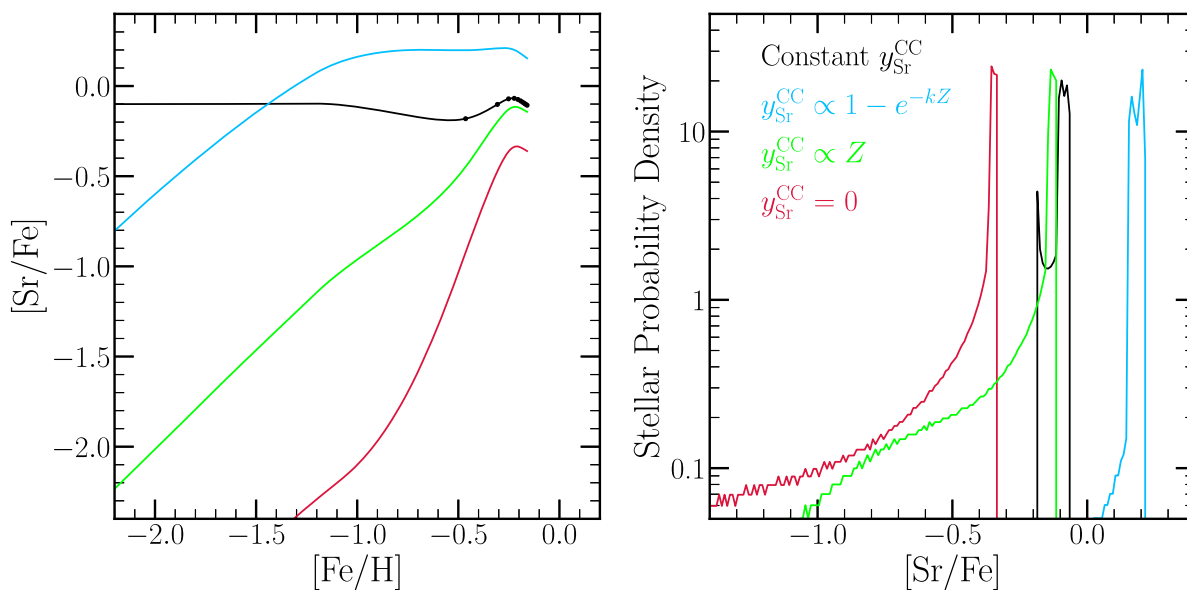


Figure 6. Evolutionary tracks (left) and final $[\text{Sr}/\text{Fe}]$ distributions (right) under our fiducial burstless GCE model for four different assumptions about $y_{\text{Sr}}^{\text{CC}}$: constant yield, zero yield, and the metallicity-dependent yields for non-rotation or rotation progenitors described by equations (11a) and (11b). The red ($y_{\text{Sr}}^{\text{CC}} = 0$) curve shows the predicted evolution for our metallicity dependent AGB yields (Cristallo et al. 2011; Fig. 5), which are adopted in all four models. On the black curve, small black points are plotted at $\Delta t = 1$ Gyr intervals, and all models reach a given $[\text{Fe}/\text{H}]$ at the same time.

4.2 Smooth evolution

Fig. 6 shows the $[\text{Sr}/\text{Fe}]$ – $[\text{Fe}/\text{H}]$ tracks and $[\text{Sr}/\text{Fe}]$ distributions for our fiducial unperturbed GCE model, with constant SFR, $\tau_* = 2$ Gyr, $\eta = 2.5$, and the AGB Sr yields illustrated in Fig. 5. We consider four different assumptions about CCSN yields: $y_{\text{Sr}}^{\text{CC}} = 0$, $y_{\text{Sr}}^{\text{CC}} = 3.5 \times 10^{-8}$, and the metallicity dependent yields of equations (11a) and (11b). The $y_{\text{Sr}}^{\text{CC}} = 3.5 \times 10^{-8}$ model has a flat plateau at $[\text{Sr}/\text{Fe}] = -0.1$ for $[\text{Fe}/\text{H}] < -1.0$, which reflects the ratio of our constant CCSN yields. The $[\text{Sr}/\text{Fe}]$ ratio then dips downward as SN Ia Fe enrichment becomes important, analogous to the knee in $[\text{O}/\text{Fe}]$ – $[\text{Fe}/\text{H}]$ evolution. However, as $[\text{Fe}/\text{H}]$ rises further, AGB enrichment becomes competitive with CCSN enrichment, and $[\text{Sr}/\text{Fe}]$ moves upward. After reaching a maximum at $[\text{Fe}/\text{H}] = -0.2$, $[\text{Sr}/\text{Fe}] = -0.1$, the $[\text{Sr}/\text{Fe}]$ curves turns downward again because the time-scale of SN Ia enrichment is longer than that of AGB enrichment. Even though single stellar populations generally produce Sr before Fe (see Fig. 5), the bulk of the Sr production in GCE follows the bulk production of more abundant elements like O and Fe due to the metallicity dependence of the yields. The $[\text{Sr}/\text{Fe}]$ distribution of this model has a peak at $[\text{Sr}/\text{Fe}] \approx -0.18$, corresponding to the minimum in the $[\text{Sr}/\text{Fe}]$ – $[\text{Fe}/\text{H}]$ curve, and a second, higher peak at $[\text{Sr}/\text{Fe}] \approx -0.1$. In detail, this second peak is split in two, corresponding to the maximum in the $[\text{Sr}/\text{Fe}]$ – $[\text{Fe}/\text{H}]$ track and the slightly lower final equilibrium.

With $y_{\text{Sr}}^{\text{CC}} = 0$ (AGB only), the $[\text{Sr}/\text{Fe}]$ ratio is below -2 for $[\text{Fe}/\text{H}] < -1$ and rises steeply with increasing $[\text{Fe}/\text{H}]$, reaching a maximum at $[\text{Sr}/\text{Fe}] \approx -0.35$. Adding CCSN enrichment with $y_{\text{Sr}}^{\text{CC}} \propto Z$, corresponding approximately to the non-rotating Limongi & Chieffi (2018) yields, gives a shallower but still steeply rising $[\text{Sr}/\text{Fe}]$ – $[\text{Fe}/\text{H}]$ trend, which peaks at $[\text{Sr}/\text{Fe}] \approx -0.1$. Although one can see the imprint of SN Ia Fe enrichment on both of these curves, it is subtle relative to the strong trend arising from metallicity-dependent CCSN yields.

Our approximate model of the rotating Limongi & Chieffi (2018) yields given by equation (11b) produces a $[\text{Sr}/\text{Fe}]$ curve

that rises rapidly until $[\text{Fe}/\text{H}] = -1$, then stays nearly constant at $[\text{Sr}/\text{Fe}] \approx +0.2$. AGB enrichment is small relative to CCSN enrichment in this model, as shown in Fig. 5. There is still a slight dip in $[\text{Sr}/\text{Fe}]$ at late times, producing a split in the $[\text{Sr}/\text{Fe}]$ distribution.

Spectra of early-type galaxies imply $[\text{Sr}/\text{Fe}] \approx 0$ for stellar populations typically dominated by solar or mildly super-solar metallicities (Conroy et al. 2013), showing that solar abundance ratios arise even in systems with very different star formation histories from the Milky Way. Measurements of individual stars in the Milky Way and in dwarf satellites show median trends that are roughly flat at $[\text{Sr}/\text{Fe}] \approx 0$ down to $[\text{Fe}/\text{H}] \approx -3$, though the star-to-star scatter becomes large below $[\text{Fe}/\text{H}] = -1$ (see e.g. Mishenina et al. 2019; Hirai, Wanajo & Saitoh 2019, and references therein). Above $[\text{Fe}/\text{H}] = -1$, our model with the Limongi & Chieffi (2018) rotating CCSN progenitor yields produces a flat $[\text{Sr}/\text{Fe}]$ trend, but only our $y_{\text{Sr}}^{\text{CC}} = \text{constant}$ model produces a flat trend to $[\text{Fe}/\text{H}]$ as low as -3 . We conclude that reproducing Milky Way observations requires an additional source of Sr that is prompt compared to SN Ia enrichment and approximately independent of metallicity at least for $[\text{Fe}/\text{H}] < -1$. This is in agreement with more detailed models of Sr enrichment investigating a variety of potential sources, such as neutron star mergers, electron-capture, and magnetorotationally-driven supernovae, and rotating massive stars (e.g. Cescutti & Chiappini 2014; Cescutti et al. 2015; Prantzos et al. 2018; Hirai et al. 2019; Rizzuti et al. 2019). Neutron-rich neutrino-driven winds from newly formed neutron stars should also produce Sr via r-process nucleosynthesis in core-collapse supernovae (Thompson, Burrows & Meyer 2001; Vlasov et al. 2017; Thompson & ud-Doula 2018), and this production is typically not included in calculations of CCSN yields such as Limongi & Chieffi (2018). Sources that produce relatively large amounts of Sr in events that are individually rare would help to explain the large star-to-star scatter at low $[\text{Fe}/\text{H}]$. We conclude that our constant $y_{\text{Sr}}^{\text{CC}} = 3.5 \times 10^{-8}$ model could retroactively account for this contribution; this arises from the nature of equation (5) which in principle could fold all prompt

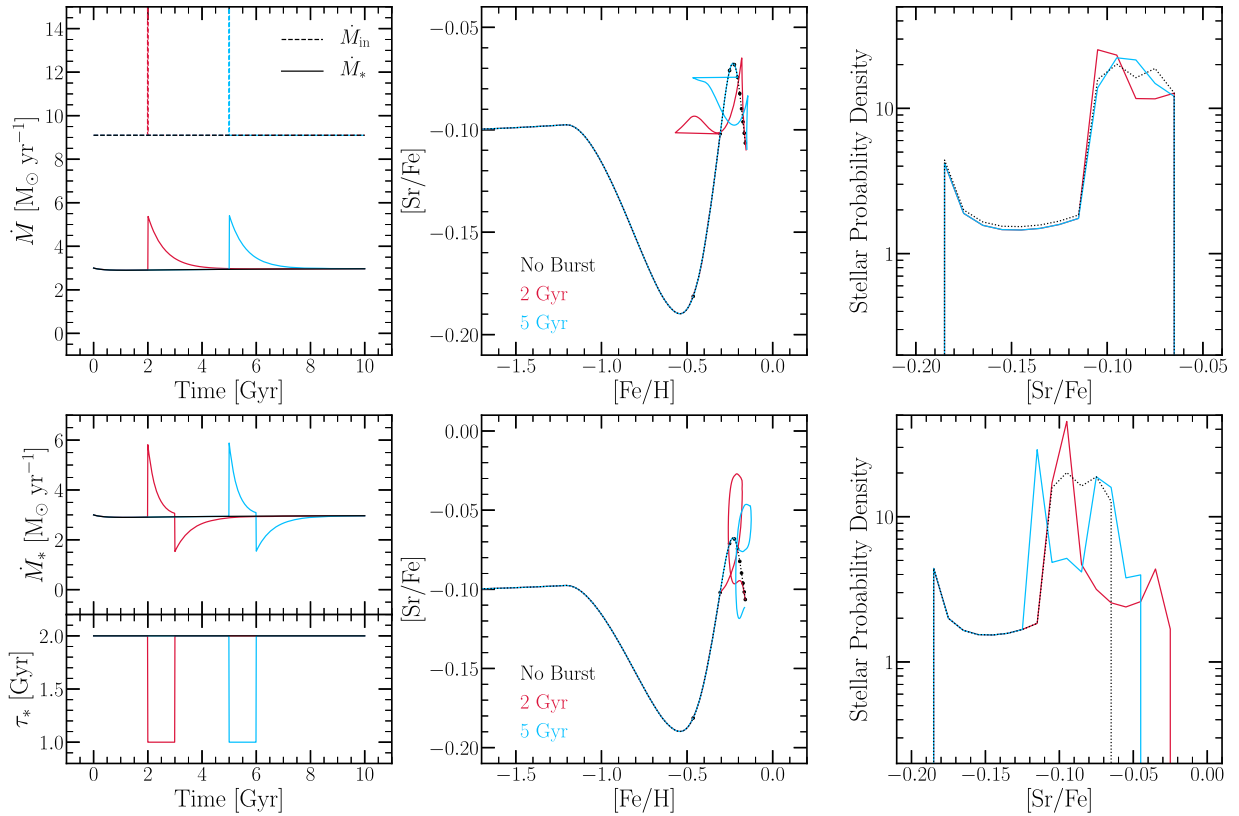


Figure 7. Evolutionary tracks (middle) and final $[\text{Sr}/\text{Fe}]$ distributions (right) for our fiducial starburst models, analogous to the top and bottom rows of Fig. 1. All models adopt $y_{\text{Sr}}^{\text{CC}} = 3.5 \times 10^{-8}$ and the Cristallo et al. (2011) AGB yields illustrated in Fig. 5.

enrichment components into $y_{\text{Sr}}^{\text{CC}}$ as a function of metallicity. None the less, we encourage caution that sufficiently accurate modelling of Sr production at metallicities as low as $[\text{Fe}/\text{H}] < -2$ may require a more complete understanding of the astrophysical origins of the r-process and the associated Sr yields.

4.3 Burst scenarios

Fig. 7 shows $[\text{Sr}/\text{Fe}]$ evolution and $[\text{Sr}/\text{Fe}]$ distributions for our fiducial gas-driven and efficiency-driven starbursts, which can be compared to the $[\text{O}/\text{Fe}]$ result in the top and bottom rows of Fig. 1. For ease of interpretation we have used the $y_{\text{Sr}}^{\text{CC}} = 3.5 \times 10^{-8}$ model for CCSN yields, and the black curves representing the unperturbed model are the same as the black curves in Fig. 6 but shown with a zoomed-in axis range. In the gas-driven models, dilution with pristine gas first drives $[\text{Fe}/\text{H}]$ lower at fixed $[\text{Sr}/\text{Fe}]$. For the burst at $t = 2$ Gyr, this backward jump is followed by a small upward hook, reminiscent of the behaviour of this model in $[\text{O}/\text{Fe}]$. However, this burst occurs very near the $[\text{Sr}/\text{Fe}]$ ratio associated with the adopted CCSN yields, suggesting that CCSNe associated with the burst do not significantly modify the ISM $[\text{Sr}/\text{Fe}]$. Instead, it is likely that this increase is due to Sr production in AGB stars from earlier epochs. Subsequently, the detailed shape of the trajectory becomes complex as both SN Ia and AGB enrichment with metallicity dependent yields become important, and eventually it rejoins the trajectory of the unperturbed model.

The $t = 5$ Gyr burst occurs after the maximum $[\text{Sr}/\text{Fe}]$, produced because a $t^{-1.1}$ SN Ia DTD produces Fe on time-scales longer than AGB stars produce Sr. In this model, $[\text{Sr}/\text{Fe}]$ initially evolves downward following the addition of zero metallicity gas, both

because of these late SNe Ia from previous generations of stars and because this is in the direction of the CCSN ratio of $[\text{Sr}/\text{Fe}] \approx -0.1$. Unfortunately, all of these excursions are small, and the impact on $[\text{Sr}/\text{Fe}]$ distributions is almost negligible. Detecting the signature of these complex tracks would require correlating precise $[\text{Sr}/\text{Fe}]$ and stellar age measurements.

The impact of efficiency-driven bursts (lower panels) is somewhat stronger. Here, the bursts drive upward excursions in $[\text{Sr}/\text{Fe}]$ because both the CCSN and AGB channels contribute Sr faster than SN Ia Fe, and the slight boost of $[\text{Fe}/\text{H}]$ increases the AGB yield. As seen previously in $[\text{O}/\text{Fe}]$, the suppressed SFR after τ_* returns to its original value causes a downward hook in $[\text{Sr}/\text{Fe}]$, as SN Ia Fe from stars produced during the burst dominates over the reduced CCSN and AGB contributions. These models produce larger deviations in the $[\text{Sr}/\text{Fe}]$ distributions than the gas-driven models, with peaks at higher and lower $[\text{Sr}/\text{Fe}]$ associated with the mid-burst maximum and post-burst minimum. However, the separation between these peaks is below 0.1 dex, so precise measurements would be needed to detect this signature.

The interpretation of Fig. 7 is complicated partly by the fact that three enrichment processes are involved: CCSN, SN Ia, and AGB. Fig. 8 examines trajectories of $[\text{Sr}/\text{O}]$ versus $[\text{O}/\text{H}]$, which are independent of SN Ia, at least given our assumption that SN Ia yields of O and Sr are insignificant. Here, we show trajectories for our two metallicity-dependent CCSN yield models as well as the constant yield model. Tracks with smooth star formation (left-hand panel) resemble the $[\text{Sr}/\text{Fe}]$ – $[\text{Fe}/\text{H}]$ tracks in Fig. 6, but without the dips coming from SN Ia Fe. For a gas-driven burst at $t = 5$ Gyr (middle panel), trajectories jump to lower $[\text{O}/\text{H}]$ through dilution, then loop downward because the burst initially raises the rate of

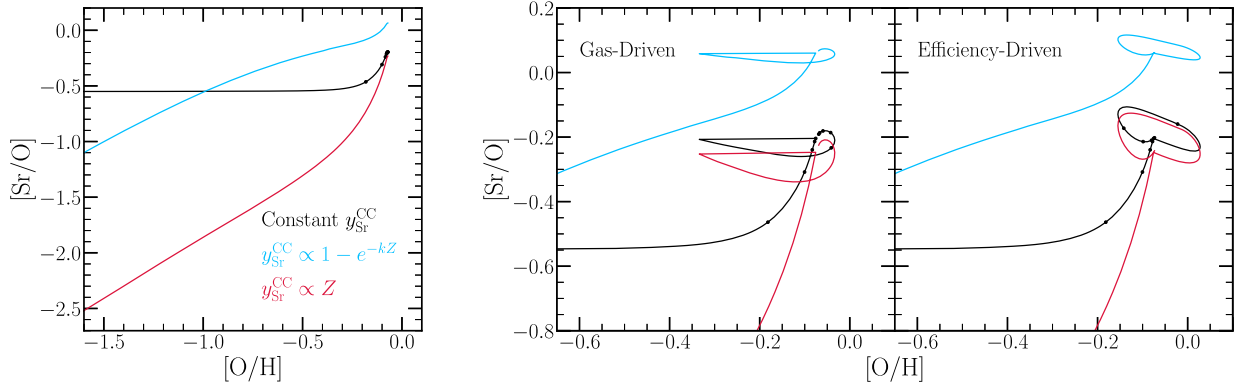


Figure 8. Evolutionary tracks in the $[\text{Sr}/\text{O}]$ – $[\text{O}/\text{H}]$ plane for our fiducial burstless model (left) and for our fiducial gas-driven (middle) or efficiency-driven (right) starburst models, for three models of the $y_{\text{Sr}}^{\text{CC}}$ yield as labelled. In contrast to Figs 6 and 7, these results are independent of SN Ia enrichment, simplifying interpretation. In the middle panels, tracks initially evolve to lower $[\text{O}/\text{H}]$ because of gas dilution, while in the right-hand panel they evolve to higher $[\text{O}/\text{H}]$ because increased SFE reduces the gas supply. The $[\text{Sr}/\text{O}]$ evolution is driven mainly by the metallicity dependence of the Sr yields. In all panels, points are plotted at 1-Gyr intervals on models shown in black.

CCSN relative to AGB enrichment. These loops are analogous to the upward loops of $[\text{O}/\text{Fe}]$, but O is now in the ratio denominator, and the time-scales are CCSN versus AGB rather than CCSN versus SN Ia. The loop is flatter for the rotating star yield model because AGB stars make a smaller fractional contribution to Sr enrichment, and the CCSN contribution is boosted for both Sr and O during the burst. All trajectories eventually return to the late-time equilibrium of the unperturbed model.

For an efficiency-driven burst at $t = 5$ Gyr (right-hand panel), evolutionary tracks have a ‘balloon-on-string’ appearance that can be understood as follows. By the time of the burst, the oxygen abundance has evolved to equilibrium, with

$$\dot{M}_{\text{O}} \approx y_{\text{O}}^{\text{CC}} \dot{M}_{*} - (1 + \eta - r_{\text{inst}}) \dot{M}_{*} (M_{\text{O}}/M_{\text{ISM}}) = 0, \quad (12)$$

where M_{O} and M_{ISM} are the oxygen and total mass in the ISM, respectively, and the oxygen abundance is

$$Z_{\text{O,eq}} = \left(\frac{M_{\text{O}}}{M_{\text{ISM}}} \right)_{\text{eq}} = \frac{y_{\text{O}}^{\text{CC}}}{1 + \eta - r_{\text{inst}}} \quad (13)$$

(WAF17, equations 11 and 14). Boosting the SFE does not initially perturb \dot{M}_{O} from zero because the sources and sinks are both proportional to \dot{M}_{*} , but the ISM gas mass decreases because of more rapid consumption, so $Z_{\text{O}} = M_{\text{O}}/M_{\text{ISM}}$ rises. The $[\text{Sr}/\text{O}]$ ratio drops slightly at first because CCSN enrichment has increased relative to AGB enrichment, but the increased metallicity boosts the AGB Sr yield, so $[\text{Sr}/\text{O}]$ loops upward once AGB enrichment from the starburst becomes important. As the burst evolves further, sinks exceed sources in equation (12), so the $[\text{O}/\text{H}]$ ratio evolves backward to lower values because $Z_{\text{O}} > Z_{\text{O,eq}}$. This evolution ‘overshoots’ the original $[\text{O}/\text{H}]$ equilibrium as the gas supply evolves back to its original value. Lower metallicity in turn leads to a drop in Sr yields and $[\text{Sr}/\text{O}]$. Eventually all models evolve back to the original pre-burst equilibrium. The loop of the $y_{\text{Sr}}^{\text{CC}} \propto Z$ model is widest in the $[\text{Sr}/\text{O}]$ dimension because for this model AGB and CCSN yields both change with metallicity, and CCSN enrichment dominates over AGB enrichment in the $y_{\text{Sr}}^{\text{CC}} \propto 1 - e^{-kZ}$ model.

Figs 7 and 8 show that the evolution of an AGB s-process element can be intricate because of both the intermediate time-scale of AGB enrichment and metallicity dependent yields. Unfortunately the perturbations of $[\text{Sr}/\text{Fe}]$ and $[\text{Sr}/\text{O}]$ ratios are relatively small, so diagnosing starbursts with these ratios will require precise abundance measurements and reasonably precise stellar ages.

5 LONG TERM MODULATION OF STAR FORMATION RATES

Bursts of star formation change the ratio of CCSNe to SNe Ia, producing loops in $[\text{O}/\text{Fe}]$ – $[\text{Fe}/\text{H}]$ trajectories and multiple peaks in $[\text{O}/\text{Fe}]$ distributions. Slower, continuous variations of SFR also perturb the CCSN/SN Ia ratio in ways that can add complexity to these trajectories and distributions. From the standpoint of starbursts, such variations can be thought of as emulating a series of minor bursts throughout a galaxy’s history, and are a possible source of scatter in $[\text{O}/\text{Fe}]$ at fixed $[\text{Fe}/\text{H}]$ in observed stellar populations. In the Milky Way disc, Bertran de Lis et al. (2016) estimate the intrinsic scatter in $[\text{O}/\text{Fe}]$ as 0.03–0.04 dex in both the high- α (‘chemical thick disc’) and low- α (‘chemical thin disc’) stellar populations.

Fig. 9 shows evolutionary tracks and $[\text{O}/\text{Fe}]$ distributions for models with sinusoidal perturbations in SFR relative to a constant SFR model. In the upper panels, we create the SFR variations by modulating the SFE time-scale τ_{*} about its baseline value of 2 Gyr. The black curve shows a model in which the amplitude of modulation is 10 per cent (i.e. 0.2 Gyr) and the period of modulation is 2 Gyr. Blue and red curves show models with a 20 per cent amplitude and a 4 Gyr period, respectively. The gas infall rate \dot{M}_{in} and the outflow efficiency η are held constant at their fiducial values.

As one might expect from our efficiency-driven starburst models, each oscillation in τ_{*} induces a low amplitude loop in the $[\text{O}/\text{Fe}]$ – $[\text{Fe}/\text{H}]$ trajectory. For a 2-Gyr period, the first minimum in SFR occurs when $[\text{Fe}/\text{H}] \approx -0.45$, and at lower metallicities the trajectory is only slightly different from that of an unperturbed model. At higher metallicities, there is a local maximum in $[\text{O}/\text{Fe}]$ associated with each maximum in SFR, as one can see from the inset in the middle panel. The resulting $[\text{O}/\text{Fe}]$ distributions have multiple peaks and troughs associated with flat and steep portions of the $[\text{O}/\text{Fe}]$ trajectories, though these peaks can merge with each other into broader features. The peaks are sharper for higher amplitude modulations as expected. For the 10 per cent modulation, 2-Gyr period model there are three distinct peaks at $[\text{O}/\text{Fe}] \approx +0.11$, $+0.15$, and $+0.20$, respectively, while the model with 4 Gyr period produces two distinct peaks at $[\text{O}/\text{Fe}] \approx +0.10$ and $+0.15$.

The lower panels of Fig. 9 show models in which we modulate the gas infall rate \dot{M}_{in} while keeping τ_{*} and η fixed. For these models we have chosen to modulate the SFR \dot{M}_{*} by 10 per cent or 20 per cent with a 2- or 4-Gyr period (solid curves in left-hand

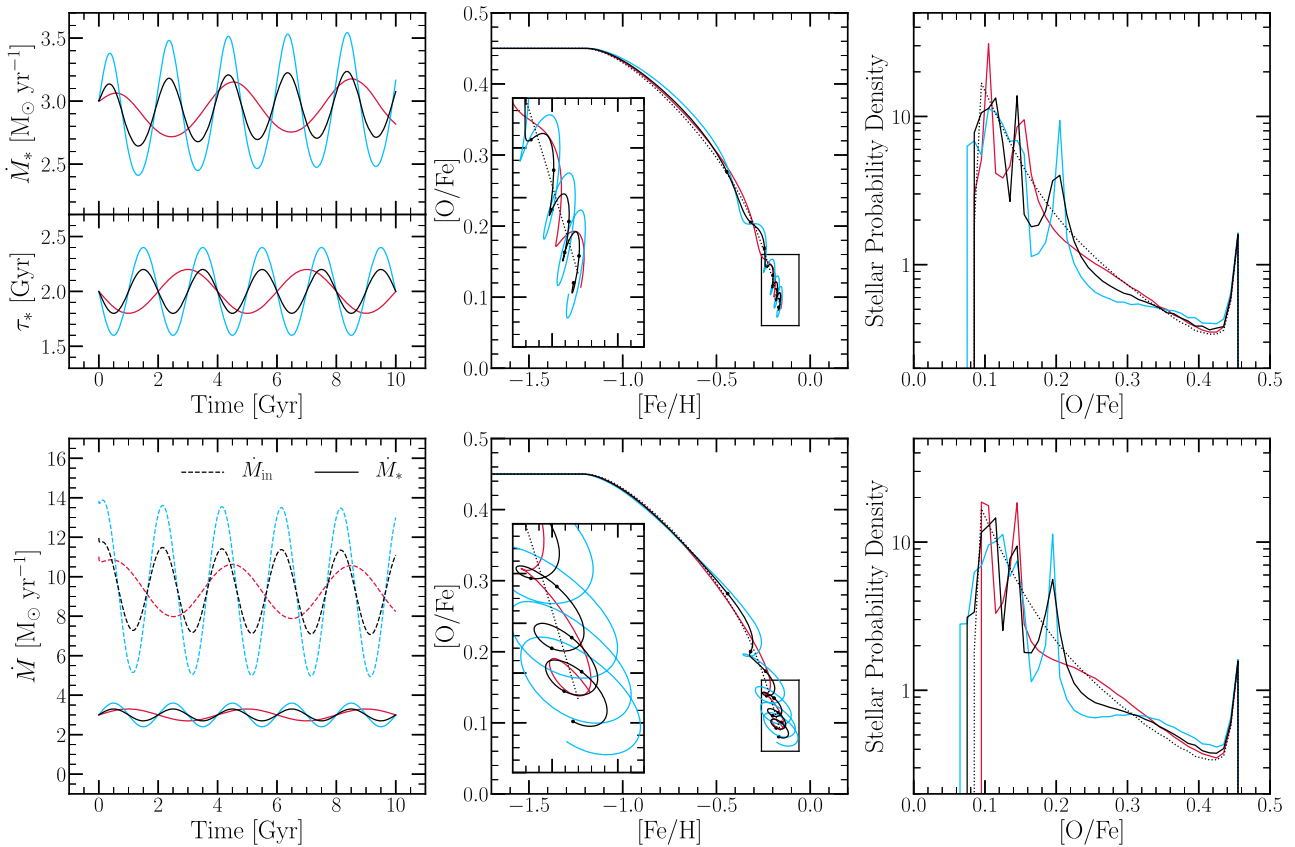


Figure 9. Models with sinusoidal modulations of the SFR induced by modulations of the SFE time-scale τ_* (top) or the gas infall rate \dot{M}_{in} (bottom). Black curves represent a model with 10 per cent SFR modulations and a 2 Gyr period, while blue and red curves show the effect of doubling the amplitude or period of the modulation, respectively. In the middle and right-hand panels, dotted black curves show results for our fiducial unperturbed model for comparison. In the middle panels, points are plotted at 1-Gyr intervals for the 10 per cent amplitude, 2-Gyr period model.

panel). VICE automatically solves for the required modulations in \dot{M}_{in} (dashed curves), which have the same period as the SFR modulations but a different phase and larger fractional amplitude. These gas supply modulations produce loops in $[\text{O}/\text{Fe}]$ trajectories that resemble those of our infall-driven burst models. In particular, trajectories first move to lower $[\text{Fe}/\text{H}]$ because of dilution, then to higher $[\text{O}/\text{Fe}]$ and $[\text{Fe}/\text{H}]$ because of subsequent star formation. The resulting $[\text{O}/\text{Fe}]$ distributions show a multipeak structure like that in the τ_* -modulation models, with peaks at similar locations.

Fig. 9 shows that moderate amplitude fluctuations (10–20 per cent) of the SFR can produce a spread of $[\text{O}/\text{Fe}]$ values at fixed $[\text{Fe}/\text{H}]$, at the ~ 0.05 -dex level. For τ_* modulations, this scatter appears mainly in the $[\text{O}/\text{Fe}]$ dimension while for \dot{M}_{in} modulations it appears in both the $[\text{O}/\text{Fe}]$ and $[\text{Fe}/\text{H}]$ dimensions, but the impact on the $[\text{O}/\text{Fe}]$ distributions is similar. This is demonstrated further in the left and middle panels of Fig. 10, which compares the 20 per cent amplitude, 2-Gyr period models of the two modes of oscillations. The middle panel shows that both modes of oscillation produce strikingly similar evolution of the ISM $[\text{O}/\text{Fe}]$ with time, but the oscillatory \dot{M}_{in} model predicts much stronger oscillations in $[\text{Fe}/\text{H}]$. These results are in good agreement with the episodic SFH model for the Milky Way bulge in Matteucci et al. (2019), which shows qualitatively similar behaviour in the $[\alpha/\text{Fe}]-[\text{Fe}/\text{H}]$ plane.

We also demonstrate in Fig. 10 that these moderate variations do not produce a bimodal distribution in $[\text{O}/\text{Fe}]$ at fixed $[\text{Fe}/\text{H}]$ as observed in the Milky Way; a more dramatic departure from this class of models is required. The right-hand panel shows the normalized

stellar MDFs in $[\text{O}/\text{Fe}]$ only considering stars with $-0.3 \leq [\text{Fe}/\text{H}] \leq -0.2$, and although these display complex structure, neither model reproduces the $[\text{O}/\text{Fe}]$ distribution found by, e.g. Bertran de Lis et al. (2016), which is well described by two Gaussians separated by ~ 0.15 dex. It is also notable that these SFR modulations only induce scatter in $[\text{O}/\text{Fe}]$ at locations well beyond the knee of the $[\text{O}/\text{Fe}]-[\text{Fe}/\text{H}]$ track. In part this is because our chosen parameters predict models which evolve past the knee quickly, before a full cycle of the SFR modulation. However, enrichment near the $[\text{O}/\text{Fe}]$ plateau is dominated by CCSN in any case, so fluctuations in the SFR that change the CCSN rate have little leverage on $[\text{O}/\text{Fe}]$. Explaining intrinsic scatter in $[\text{O}/\text{Fe}]$ (or ratios for other α -elements) near the plateau of the high- α sequence requires a different mechanism, such as incomplete mixing of CCSN ejecta that individually have varying $[\text{O}/\text{Fe}]$ ratios.

6 SLOW STARBURST IN THE MILKY WAY

Although our starburst models are most obviously relevant to dwarf galaxies with episodic star formation histories, some recent observations suggest that the Milky Way itself experienced substantially elevated star formation 2–3 Gyr ago. Mor et al. (2019) infer such a history by comparing population synthesis models to observed stellar luminosity functions and colour–magnitude diagrams from *Gaia* data. Isern (2019) reaches similar conclusions from modelling the luminosity function of white dwarfs in the solar neighborhood measured using *Gaia* parallaxes. Although these white dwarfs are

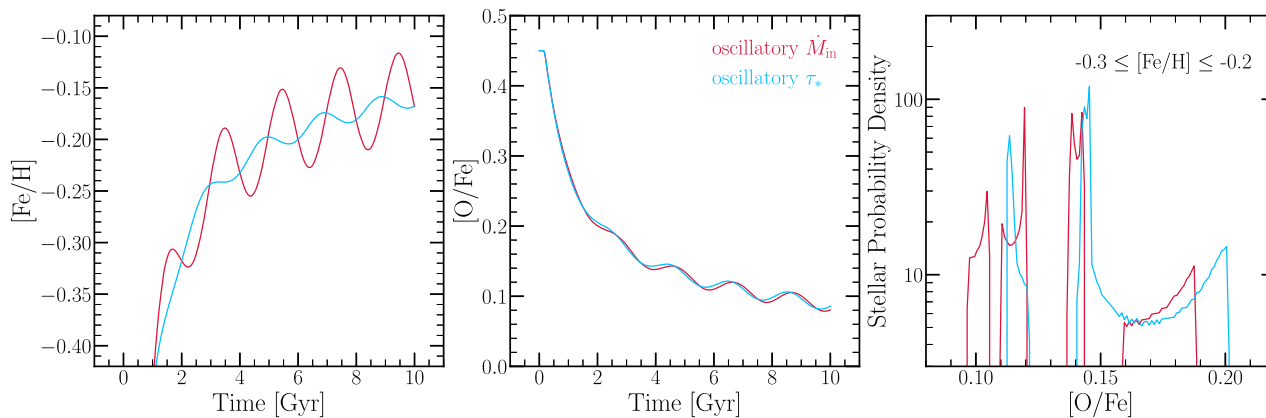


Figure 10. Time evolution of $[\text{Fe}/\text{H}]$ (left) and $[\text{O}/\text{Fe}]$ (middle) for the 20 percent amplitude, 2-Gyr models driven by τ_* modulations (red curves) or \dot{M}_{in} modulations (blue curves). Oscillations of $[\text{Fe}/\text{H}]$ are larger in the infall modulation model, but oscillations of $[\text{O}/\text{Fe}]$ are similar in the two models. The right-hand panel shows the $[\text{O}/\text{Fe}]$ distributions for stars in the range $-0.2 \leq [\text{Fe}/\text{H}] \leq -0.3$, demonstrating that at constant $[\text{Fe}/\text{H}]$, the resultant $[\text{O}/\text{Fe}]$ distribution is not a simple bimodal Gaussian.

close to the sun, dynamical mixing implies that they at least sample the history of the solar annulus, and older white dwarfs likely sample a range of Galactocentric radii because of radial mixing. Resolved stellar population studies of the M31 disc also provide evidence for elevated star formation 2–4 Gyr ago with much lower SFR before and after (Williams et al. 2017, figs 22–23).

Fig. 11 presents the evolution of two models loosely motivated by these observations. The first (blue curves) has a constant SFR to which we have added a burst described by a Gaussian centred at $t = 12$ Gyr (lookback time 2 Gyr) with dispersion of 1 Gyr. At its peak, this burst approximately doubles the galaxy SFR relative to the pre-burst value. The second model (red curve) adds a similar burst to a model with an infall history described by $\dot{M}_{\text{in}} \propto t^2 e^{-t}$ with e -folding time-scale $\tau_{\text{inf}} = 2.2$ Gyr. The pre-burst SFR first climbs as the gas supply builds (starting from zero), then declines as the infall rate slows. The qualitative appearance of this model is similar to those in fig. (1) of Isern (2019). For both models we adopt $\eta = 2.5$ and $\tau_* = (2 \text{ Gyr})(M_g/6.0 \times 10^9 M_\odot)^{-0.5}$, allowing VICE to solve for the infall rate required to produce the starburst. We also plot the evolution of the corresponding quiescent models in dotted lines for comparison; they follow the same evolution but with no added starburst.

The $[\text{O}/\text{Fe}]$ – $[\text{Fe}/\text{H}]$ tracks show loops similar to those of our infall-driven and efficiency-driven burst models (e.g. Fig. 1) and qualitatively resemble that of Spitoni et al. (2019), who investigated similar models for the solar annulus in much greater detail. As found in previous studies (AWSJ17, WAF17), the exponential infall model exhibits slower pre-burst evolution and a more gradual ‘knee’, and because of the short e -folding time-scale even the unperturbed model does not approach equilibrium by $t = 14$ Gyr. The critical feature of these models relative to our fiducial starbursts is that the effects of the bursts have not decayed by the end of the simulations at $t = 14$ Gyr. Over the final 2 Gyr, the values of $[\text{O}/\text{H}]$ and $[\text{Fe}/\text{H}]$ are rapidly climbing and end at values higher than those reached at any previous time. The $[\text{O}/\text{Fe}]$ values in both models reach a local maximum at $t = 12$ Gyr, then fall for the final 2 Gyr.

These results are of particular interest in light of recent studies of age-abundance relations from the Apache Point Observatory Galaxy Evolution Experiment (APOGEE; e.g. Martig et al. 2016; Feuillet et al. 2018, 2019; Silva Aguirre et al. 2018). The late bump in $[\text{O}/\text{Fe}]$ could help explain populations of young α -enhanced stars (Martig et al. 2016; Feuillet et al. 2019), though in these models such stars would have modest α -enhancements, near-solar metallicity, and age

≈ 2 Gyr. The late-time bumps in $[\text{O}/\text{H}]$ and $[\text{Fe}/\text{H}]$ could help to explain the strikingly young (1–2 Gyr) median ages that Feuillet et al. (2018) find for solar neighborhood stars with $[\text{Fe}/\text{H}] \approx 0$ or $[\text{O}/\text{H}] \approx 0$. Finally, the most α -poor stars predicted by these models form at late times in the wake of the burst, potentially explaining the low median age (~ 1 Gyr) that Feuillet et al. (2018) find for stars with $[\alpha/\text{Fe}] < 0$. The age–metallicity relation for solar neighborhood stars exhibits large scatter (Edvardsson et al. 1993), and explaining this scatter likely requires radial mixing of stellar populations (e.g. Schönrich & Binney 2009) or some other mechanism not represented in one-zone GCE models. However, while multizone models with radial mixing and smooth star formation histories can explain a large dispersion in age-abundance relations, they still have difficulty reproducing the young median ages inferred for solar metallicity stars (Feuillet et al. 2018, see their fig. 15). The one-zone models presented here suggest that elevated star formation in the recent past could have a significant impact on age-abundance relations, pushing them away from the equilibrium behaviour predicted for smooth star formation histories. Furthermore, the differences between these models and their corresponding quiescent cases at late times raise the intriguing possibility that the recent burst in the Milky Way has not yet fully decayed. This would imply that the present-day chemistry of the Milky Way is still mildly perturbed due to the recent starburst. We reserve an exploration of models combining radial mixing with star formation histories like those of Mor et al. (2019) and Isern (2019) for future work.

7 CONCLUSION

We have studied one-zone chemical evolution models tracking the enrichment of oxygen, iron, and strontium with the goal of understanding the impact of star formation bursts on elemental abundance ratios. To this end, we have developed the Versatile Integrator for Chemical Evolution (VICE), a python package optimized for handling highly non-linear chemical evolution models. With this new tool, we first simulated gas-driven starbursts, whereby an amount of gas comparable to the current ISM mass of a galaxy is added to the ISM on time-scales shorter than the depletion time. These starburst models predict hooks in the $[\text{O}/\text{Fe}]$ – $[\text{Fe}/\text{H}]$ plane; the rapid addition of pristine gas first causes a reduction in $[\text{Fe}/\text{H}]$ at fixed $[\text{O}/\text{Fe}]$, then the elevated rate of CCSNe relative to SNe Ia

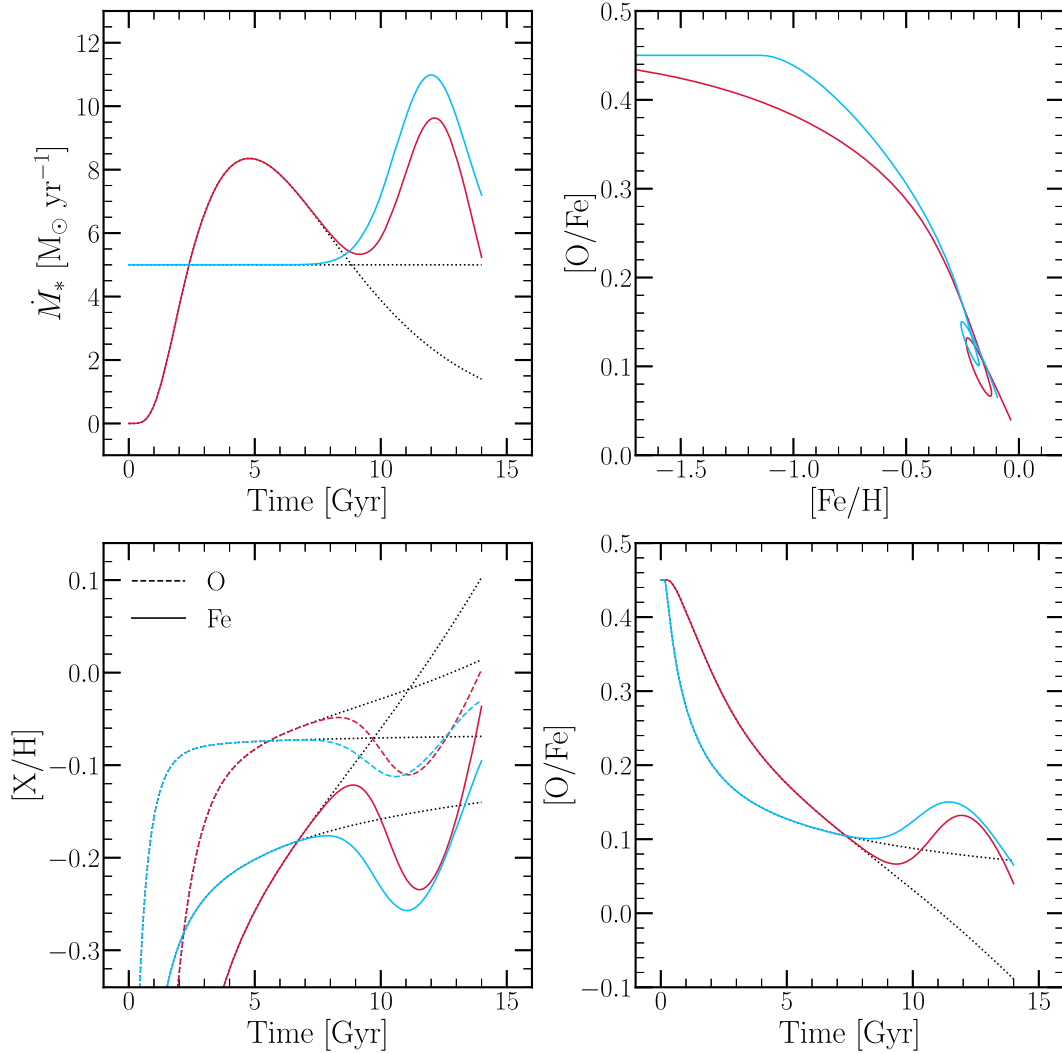


Figure 11. Models loosely motivated by recent findings of a slow starburst in the Milky Way ~ 2 Gyr ago (Isern 2019; Mor et al. 2019). These models exhibit a constant SFR (blue) and a $\propto t^2 e^{-t}$ infall history (red), to which we add a Gaussian centred at $t = 12$ Gyr with dispersion $\sigma = 1$ Gyr to both models, roughly doubling the SFR at its peak. Black dotted lines in all panels show the corresponding quiescent scenario, to which we add no starburst. *Top left:* The SFR as a function of time. *Top right:* The [O/Fe]–[Fe/H] tracks. We omit the tracks of the quiescent model from this panel for clarity. *Bottom left:* [O/H] (dashed) and [Fe/H] (solid) as a function of time. *Bottom right:* [O/Fe] as a function of time. These models produce mildly α -enhanced stars with young ages and a low median age of stars near solar metallicity.

drives the ISM to higher [O/Fe] and [Fe/H], and finally the onset of SNe Ia associated with the starburst pushes the ISM back towards the [O/Fe]–[Fe/H] track of the unperturbed (i.e. no-burst) model. The rate at which extra gas is added to the galaxy affects the detailed shape of these jump-and-hook trajectories. Although this paper focuses on characterizing model predictions rather than interpreting data, we provide an illustrative comparison to Kirby et al.’s (2010) abundance measurements for Milky Way dwarf satellites in Appendix A.

Our unperturbed constant-SFR models predict one peak in the [O/Fe] distribution at the ‘plateau’ ratio of CCSN O and Fe yields, and a second peak associated with the late-time equilibrium in which CCSN and SN Ia rates are equal. Our gas-driven starburst models predict a third peak in the [O/Fe] distribution, associated with stars that form out of the α -enhanced ISM during/after the burst before SNe Ia have driven evolution back towards the unperturbed evolutionary track. The peak is centred near the value of [O/Fe] at the top of the hook in the [O/Fe]–[Fe/H] trajectory, and its location and shape are insensitive to the time-scale on which

the gas is added, provided that this time-scale is short compared to the depletion time. Earlier starbursts produce this third peak at higher [O/Fe] because they arise when the starting value of [O/Fe] is further from its eventual equilibrium. Thus, even without accurate ages for individual stars, the existence of extra peaks in the [O/Fe] distribution (or [X/Fe] distribution for other α -elements) can provide an observable diagnostic for past bursts of galactic star formation, and the locations of these peaks can provide estimates of the timing of these bursts.

A gas-driven starburst could arise from the merger of a gas rich system or a temporary increase in accretion rate. A starburst can also arise from a temporary increase in SFE, consuming the available gas more quickly, perhaps because of a dynamical disturbance that does not increase the gas supply. The evolutionary tracks of efficiency-driven starbursts differ in form from those of gas-driven starbursts, first because there is no drop in [Fe/H] before the increase in [O/Fe], and second because [O/Fe] loops below the track of the unperturbed model once the post-burst gas supply is depleted, which allows the

CCSN rate to fall well below the rate of SNe Ia from stars that formed during the burst. With sufficiently precise data, the [O/Fe] distribution of an efficiency-driven burst can be distinguished from that of a gas-driven burst, in part by the shape of the [O/Fe] peak for α -enhanced stars formed during the burst, and in part by the presence of an additional population of α -deficient stars.

In short, the chemical response to a simple starburst is driven by a perturbation of the CCSN and SN Ia rates. Conventionally, one-zone models tie the outflowing wind to the instantaneous SFR (i.e. $\dot{M}_{\text{out}} = \eta \dot{M}_*$), which in turn ties it to the CCSN rate. If SNe Ia contribute to the outflowing wind, then a better approximation of the outflow rate would be one that is tied to a time-averaged SFR (i.e. $\dot{M}_{\text{out}} = \eta \langle \dot{M}_* \rangle_{\tau_s}$), where τ_s is the outflow smoothing time. Non-zero τ_s allows the ISM to retain more gas at the onset of a starburst, because the outflow is more sensitive to the preburst SFR. The ISM is then gas poor in the decay of the starburst, because the outflow is most sensitive to the elevated SFR from the recent burst. Varying τ_s between 0 and 1 Gyr has minimal impact on the predicted [O/Fe]–[Fe/H] trajectory or the stellar [O/Fe] distribution of gas-driven starbursts. However, efficiency-driven burst models with $\tau_s = 0.5$ –1 Gyr exhibit wider loops and produce lower $[\alpha/\text{Fe}]$ stars than in the $\tau_s = 0$ model. These α -deficient stars are produced late in the burst when the ISM is gas poor, an effect that is magnified by a non-zero τ_s because the gas outflow rate is higher and the CCSN rate is lower.

While our simplest starburst scenarios are either gas- or efficiency-driven, there is observational evidence for starbursts driven by both an increase in the gas supply and an increase in the efficiency (Kennicutt & Evans 2012, and the citations therein). As a simple example of a ‘hybrid’ starburst, we considered a model with a rapid influx of gas and an SFE time-scale $\tau_* \propto M_g^{-1/2}$ as suggested by the Kennicutt–Schmidt law (Schmidt 1959, 1963; Kennicutt 1998). For $\tau_s = 0$ or 0.5 Gyr, the [O/Fe]–[Fe/H] tracks of this model are nearly the same as those of the gas-driven constant- τ_* model. For $\tau_s = 1$ Gyr, the hybrid model shows aspects of both gas-driven and efficiency-driven models, including a population of α -deficient stars.

The AGB models of Cristallo et al. (2011) predict Sr yields that are strongly dependent on metallicity and dominated by 2–4 M_\odot stars. Predicted CCSN yields of Sr are sensitive to rotationally induced mixing; the Limongi & Chieffi (2018) yield for non-rotating progenitors versus progenitors with $v_{\text{rot}} = 150 \text{ km s}^{-1}$ differ by 1–2 orders of magnitude, with strong but differing metallicity dependence. Near solar metallicity, the AGB yields and non-rotating CCSN yields are comparably important, but the $v_{\text{rot}} = 150 \text{ km s}^{-1}$ CCSN yields would outweigh AGB yields by a large factor.

Reproducing the approximately flat trend of [Sr/Fe] versus [Fe/H] found in the Milky Way and in dwarf satellites (Hirai et al. 2019; Mishenina et al. 2019) requires an additional source of Sr with a yield that is nearly independent of metallicity, perhaps the neutrino-driven winds from newly formed neutron stars (Thompson et al. 2001; Vlasov et al. 2017; Thompson & ud-Doula 2018). For any of these CCSN yield models, the tracks of [Sr/Fe] versus [Fe/H] in starburst models are complex, affected by the yield metallicity dependence and by the differing time-scales of CCSN, AGB, and SN Ia enrichment. Tracks of [Sr/O] versus [O/H] are simpler because they are independent of SN Ia enrichment. However, the total range of [Sr/Fe] or [Sr/O] induced by starbursts is small, typically 0.05–0.1 dex, and in combination with yield uncertainties this small dynamic range makes it difficult to use Sr abundances as a diagnostic of starburst behaviour.

In addition to strong (factor of ~ 2) starbursts, we have investigated models with 10–20 per cent sinusoidal modulations of a constant SFR, induced by variations in infall rate or SFE. These models

predict [O/Fe]–[Fe/H] tracks that oscillate about the prediction of the constant SFR model. They produce a multi-peaked structure in [O/Fe] distributions, though in the presence of observational errors these peaks would likely merge into a broader distribution. These variations do not produce a bimodal [O/Fe] distribution, so they are not the origin of the observed separation of thin and thick-disc sequences (e.g. Bensby et al. 2003; Hayden et al. 2015; Bertran de Lis et al. 2016). However, moderate variations in SFR could be a source of scatter in [O/Fe] along these sequences. With our adopted parameter values, our smooth evolution models approximately reproduce the observed high- α sequence. SFR oscillations produce a spread of ~ 0.05 – 0.1 dex in [O/Fe] for [Fe/H] $\gtrsim -0.4$, but they cannot produce scatter near the high- α plateau of this sequence because the enrichment of those stars is dominated by CCSN in any case.

Motivated by findings on the recent star formation history of the Milky Way by Mor et al. (2019) and Isern (2019), we explored models that exhibit slow, factor of ~ 2 increases in the SFR at lookback times of ~ 2 Gyr, adopting a simple Gaussian with dispersion of $\sigma = 1$ Gyr to describe the starburst. A late-time, slow starburst may help to explain otherwise puzzling features of the age-abundance relations observed in APOGEE (Martig et al. 2016; Feuillet et al. 2018, 2019; Silva Aguirre et al. 2018), such as young stars with mild α -enhancements and young median ages of solar metallicity or α -deficient stars. Complete modelling of these observables requires multizone models that account for radial mixing of stellar populations, and we reserve such investigations to future work.

Throughout this paper we have adopted an O yield similar to those predicted by Chieffi & Limongi (2004, 2013), assuming a Kroupa IMF in which all stars with $M > 8 M_\odot$ explode. With this yield, evolving to solar metallicity requires fairly strong outflows, with $\eta = 2.5$ (e.g. Finlator & Davé 2008; Peebles & Shankar 2011; AWSJ17, WAF17). With lower IMF-averaged SN yields, which could arise if many massive stars form black holes instead of exploding, lower values of η would be needed to reach the same final metallicity. Results for lower yield, lower η models would differ in detail from those presented here, mainly because the depletion time $\tau_{\text{dep}} = \tau_*/(1 + \eta - r_{\text{inst}})$ would be longer for the same τ_* . However, we have investigated several of our models in which both yields and η are reduced by a factor of ~ 2 and found that our qualitative conclusions still hold.

We have released VICE as open-source software under the MIT license. Source code, installation instructions, and documentation can be found at <http://github.com/giganano/VICE.git>. We also include code that runs the simulations of our models and produces the figures in this paper.

ACKNOWLEDGEMENTS

We are grateful to the anonymous referee for valuable and insightful comments on our analysis. We thank Jenna Freudenburg, Jennifer Johnson, Tuguldur Sukhbold, Todd Thompson, and Fiorenzo Vincenzo for helpful advice. This work was supported by National Science Foundation grants AST-1211853 and AST-1909841 and by an Ohio State University graduate fellowship.

DATA AVAILABILITY

Both the source code for all simulations and figures presented in this paper and the Kirby et al. (2010) data employed in Appendix A are available in VICE’s GitHub repository at <https://github.com/giganano/VICE/tree/master/starbursts>. Instructions on how to run the code to produce the figures can be found there as well.

REFERENCES

- Adams S. M., Kochanek C. S., Gerke J. R., Stanek K. Z., Dai X., 2017, *MNRAS*, 468, 4968
- Andrews B. H., Martini P., 2013, *ApJ*, 765, 140
- Andrews B. H., Weinberg D. H., Schönrich R., Johnson J. A., 2017, *ApJ*, 835, 224 (AWSJ17)
- Asplund M., Grevesse N., Sauval A. J., Scott P., 2009, *ARA&A*, 47, 481
- Bensby T., Feltzing S., Lundström I., 2003, *A&A*, 410, 527
- Bertran de Lis S. et al., 2016, *A&A*, 590, A74
- Bilitewski T., Schönrich R., 2012, *MNRAS*, 426, 2266
- Brown J. S. et al., 2019, *MNRAS*, 484, 3785
- Cescutti G., Chiappini C., 2014, *A&A*, 565, A51
- Cescutti G., Romano D., Matteucci F., Chiappini C., Hirschi R., 2015, *A&A*, 577, A139
- Chieffi A., Limongi M., 2004, *ApJ*, 608, 405
- Chieffi A., Limongi M., 2013, *ApJ*, 764, 21
- Chisholm J., Tremonti C., Leitherer C., 2018, *MNRAS*, 481, 1690
- Clarke A. J. et al., 2019, *MNRAS*, 484, 3476
- Conroy C., van Dokkum P. G., Graves G. J., 2013, *ApJ*, 763, L25
- Cristallo S. et al., 2011, *ApJS*, 197, 17
- Dalcanton J. J., 2007, *ApJ*, 658, 941
- Edvardsson B., Andersen J., Gustafsson B., Lambert D. L., Nissen P. E., Tomkin J., 1993, *A&A*, 500, 391
- Feuillet D. K. et al., 2018, *MNRAS*, 477, 2326
- Feuillet D. K., Frankel N., Lind K., Frinchaboy P. M., García-Hernández D. A., Lane R. R., Nitschelm C., Roman-Lopes A. r., 2019, *MNRAS*, 489, 1742
- Finlator K., Davé R., 2008, *MNRAS*, 385, 2181
- Freudenburg J. K. C., Weinberg D. H., Hayden M. R., Holtzman J. A., 2017, *ApJ*, 849, 17
- Frischknecht U. et al., 2016, *MNRAS*, 456, 1803
- Gerke J. R., Kochanek C. S., Stanek K. Z., 2015, *MNRAS*, 450, 3289
- Gilmore G., Wyse R. F. G., 1991, *ApJ*, 367, L55
- Hayden M. R. et al., 2015, *ApJ*, 808, 132
- Hirai Y., Wanajo S., Saitoh T. R., 2019, *ApJ*, 885, 33
- Isern J., 2019, *ApJ*, 878, L11
- Iwamoto K., Brachwitz F., Nomoto K., Kishimoto N., Umeda H., Hix W. R., Thielemann F.-K., 1999, *ApJS*, 125, 439
- Kalirai J. S., Hansen B. M. S., Kelson D. D., Reitzel D. B., Rich R. M., Richer H. B., 2008, *ApJ*, 676, 594
- Karakas A. I., 2010, *MNRAS*, 403, 1413
- Kennicutt Jr. R. C., 1998, *ApJ*, 498, 541
- Kennicutt R. C., Evans N. J., 2012, *ARA&A*, 50, 531
- Kirby E. N. et al., 2010, *ApJS*, 191, 352
- Kroupa P., 2001, *MNRAS*, 322, 231
- Krumholz M. R., Ting Y.-S., 2018, *MNRAS*, 475, 2236
- Lacey C. G., Fall S. M., 1985, *ApJ*, 290, 154
- Larson R. B., 1972, *Nat. Phys. Sci.*, 236, 7
- Leroy A. K., Walter F., Brinks E., Bigiel F., de Blok W. J. G., Madore B., Thornley M. D., 2008, *AJ*, 136, 2782
- Limongi M., Chieffi A., 2018, *ApJS*, 237, 13
- Maoz D., Graur O., 2017, *ApJ*, 848, 25
- Maoz D., Mannucci F., 2012, *PASA*, 29, 447
- Martig M. et al., 2016, *MNRAS*, 456, 3655
- Matteucci F., Francois P., 1989, *MNRAS*, 239, 885
- Matteucci F., Grisoni V., Spitoni E., Zulianello A., Rojas-Arriagada A., Schultheis M., Ryde N., 2019, *MNRAS*, 487, 5363
- Minchev I., Steinmetz M., Chiappini C., Martig M., Anders F., Matijevic G., de Jong R. S., 2017, *ApJ*, 834, 27
- Mishenina T., Pignatari M., Gorbaneva T., Bisterzo S., Travaglio C., Thielemann F. K., Soubiran C., 2019, *MNRAS*, 484, 3846
- Mor R., Robin A. C., Figueras F., Roca-Fàbrega S., Luri X., 2019, *A&A*, 624, L1
- Peebles M. S., Shankar F., 2011, *MNRAS*, 417, 2962
- Pejcha O., Thompson T. A., 2015, *ApJ*, 801, 90
- Petit A. C., Krumholz M. R., Goldbaum N. J., Forbes J. C., 2015, *MNRAS*, 449, 2588
- Prantzos N., Abia C., Limongi M., Chieffi A., Cristallo S., 2018, *MNRAS*, 476, 3432
- Rizzuti F., Cescutti G., Matteucci F., Chieffi A., Hirschi R., Limongi M., 2019, *MNRAS*, 489, 5244
- Schmidt M., 1959, *ApJ*, 129, 243
- Schmidt M., 1963, *ApJ*, 137, 758
- Schönrich R., Binney J., 2009, *MNRAS*, 396, 203
- Seitzzahl I. R. et al., 2013, *MNRAS*, 429, 1156
- Silva Aguirre V. et al., 2018, *MNRAS*, 475, 5487
- Spitoni E., Silva Aguirre V., Matteucci F., Calura F., Grisoni V., 2019, *A&A*, 623, A60
- Sukhbold T., Ertl T., Woosley S. E., Brown J. M., Janka H.-T., 2016, *ApJ*, 821, 38
- Thompson T. A., ud-Doula A., 2018, *MNRAS*, 476, 5502
- Thompson T. A., Burrows A., Meyer B. S., 2001, *ApJ*, 562, 887
- Tinsley B. M., 1980, *Fund. Cosmic Phys.*, 5, 287
- Vlasov A. D., Metzger B. D., Lippuner J., Roberts L. F., Thompson T. A., 2017, *MNRAS*, 468, 1522
- Weinberg D. H., Andrews B. H., Freudenburg J., 2017, *ApJ*, 837, 183 (WAF17)
- Weisz D. R. et al., 2011, *ApJ*, 739, 5
- Weisz D. R., Dolphin A. E., Skillman E. D., Holtzman J., Gilbert K. M., Dalcanton J. J., Williams B. F., 2014, *ApJ*, 789, 147
- Williams B. F. et al., 2017, *ApJ*, 846, 145
- Woosley S. E., Weaver T. A., 1995, *ApJS*, 101, 181
- Zahid H. J., Bresolin F., Kewley L. J., Coil A. L., Davé R., 2012, *ApJ*, 750, 120

APPENDIX A: EXAMPLE COMPARISON TO OBSERVATIONAL DATA

In this section, we demonstrate a comparison between model predictions as calculated by *VICE* and observational data, taking the catalogue of stars in Milky Way dwarf satellite galaxies from Kirby et al. (2010) as an example. We clarify that we are not modelling the observational data in detail to derive conclusions about how these dwarf galaxies evolved, but rather illustrate how one might go about using *VICE* to do so as well as to connect the results presented in this work to what is observed in nature.

The Kirby et al. (2010) sample consists of 2961 stars from eight dwarf satellite galaxies of the Milky Way: Sculptor, Fornax, Leo I, Sextans, Leo II, Canes Ventatici I, Ursa Minor, and Draco. They derive abundances of Fe, Mg, Si, Ca, and Ti through Keck/DEIMOS medium-resolution spectroscopy combined with spectral synthesis. For demonstration purposes, we cut the sample by removing all stars that do not have measurements for all five of these elements, resulting a sample of 849 stars. Our final sample thus consists of stars from each of these dwarf galaxies with the exception of Fornax, for which no star meets this requirement.

In Fig. A1, we plot this sample in the $[\text{Mg}/\text{Fe}]$ – $[\text{Fe}/\text{H}]$ plane. These stars are at significantly subsolar metallicities, which is expected given the low stellar masses of these galaxies and the observed mass–metallicity relation (e.g. Andrews & Martini 2013). The error bar in the lower left corner illustrates the median uncertainties in $[\text{Fe}/\text{H}]$ and $[\text{Mg}/\text{Fe}]$ for the Ursa Minor sample. This demonstrates that a significant portion of the scatter in these data is due to large observational uncertainties. In principle, there should also be some level of physical scatter due to the time-scale for mixing of newly produced metals in the ISM, an effect which is deliberately neglected by the instantaneous mixing approximation. Different dwarfs could also be offset because of differences in SFE, outflows, etc.

While the Kirby et al. (2010) sample does not provide abundances of O, which our analysis has focused on thus far as the representative α element, Mg is also an α element and can be interpreted similarly.

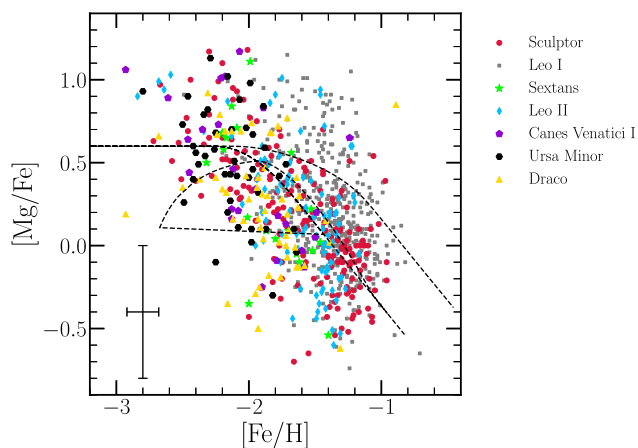


Figure A1. A comparison of three chemical evolution models simulated by VICE to the data obtained by Kirby et al. (2010). All model predictions are plotted in a dashed black line, while the coloured points with various symbols correspond to various dwarf galaxies as indicated by the legend. The error bar in the lower left shows the median error in $[\text{Fe}/\text{H}]$ and the median error in $[\text{Mg}/\text{Fe}]$ for the Ursa Minor sample. The model prediction with the highest final $[\text{Fe}/\text{H}]$ corresponds to one with an initial ISM mass of $0 M_{\odot}$, an exponential infall history with e-folding time-scale $\tau_{\text{in}} = 2$ Gyr ($\dot{M}_{\text{in}} = 9.1 M_{\odot} \text{ yr}^{-1}$ at $t = 0$), SFE time-scale of $\tau_{*} = 10$ Gyr, and mass loading factor $\eta = 30$. The lower metallicity models correspond to the same parameters with an outflow enhancement factor $\xi_{\text{enh}} = 3$ (i.e. $Z_{\text{outflow}} = 3Z_{\text{ISM}}$). The third and final model is one in which $5 \times 10^9 M_{\odot}$ of $Z = 0$ gas is added at $t = 5$ Gyr, similar to the gas-driven starburst models explored in the top panel of Fig. 1.

We therefore adopt $y_{\text{Mg}}^{\text{la}} = 0$ similar to O, and a value of $y_{\text{Mg}}^{\text{CC}}$ such that $[\text{Mg}/\text{Fe}] = 0.6$ at low $[\text{Fe}/\text{H}]$. In that regime, $[\text{Mg}/\text{Fe}]$ is set by the ratio of yields from CCSN-dominated enrichment, namely:

$$[\text{Mg}/\text{Fe}]_{\text{CC}} = \log_{10} \left(\frac{y_{\text{Mg}}^{\text{CC}}}{y_{\text{Fe}}^{\text{CC}}} \right) - \log_{10} \left(\frac{Z_{\text{Mg},\odot}}{Z_{\text{Fe},\odot}} \right), \quad (\text{A1})$$

where the yields are again defined by equation (6). By specifying $[\text{Mg}/\text{Fe}]_{\text{CC}} = 0.6$, adopting $y_{\text{Fe}}^{\text{CC}} = 0.0012$ as in this work, and the solar abundances measured by Asplund et al. (2009), this equation

dictates $y_{\text{Mg}}^{\text{CC}} = 0.00261$. This value is not calculated using yield tables from supernova nucleosynthesis studies as in previous sections, and is instead adopted in the interest of obtaining a simple model which may accurately describe these galaxies.

We next define a one-zone chemical evolution model with an initial ISM mass of $0 M_{\odot}$, an exponential infall history with e-folding time-scale $\tau_{\text{in}} = 2$ Gyr, SFE time-scale $\tau_{*} = 10$ Gyr, and mass-loading factor $\eta = 30$. This model is plotted over the Kirby et al. (2010) sample in Fig. A1, and extends to higher $[\text{Fe}/\text{H}]$ than the observational sample. We then modify this model with an outflow enhancement factor $\xi_{\text{enh}} = 3$ (i.e. the outflows are 3 times the metallicity of the ISM), motivated by the observations of Chisholm, Tremonti & Leitherer (2018) which suggest that dwarf galaxies have metal-rich outflows relative to their interstellar media. This model reaches lower $[\text{Fe}/\text{H}]$ at late times and slightly lower $[\text{Mg}/\text{Fe}]$, in better agreement with the data from all of these galaxies. The metal-weighted outflow mass-loading required to achieve this agreement, $\xi_{\text{enh}}\eta = 90$, is high. However, it is a plausible extrapolation of the mass/metal-loading trends required to match, e.g. the observed mass–metallicity relation (Finlator & Davé 2008; Peebles & Shankar 2011) to the mass range $M_{*} \sim 10^6\text{--}10^7 M_{\odot}$ of the dwarfs.

We further modify this model to exhibit a starburst at $t = 5$ Gyr in a similar manner as the models explored in the top row of Fig. 1, namely:

$$\dot{M}_{\text{in}} = \begin{cases} 5000 M_{\odot} \text{ yr}^{-1} & (5 \text{ Gyr} < t < 5.001 \text{ Gyr}) \\ 9.1 e^{-t/(2 \text{ Gyr})} M_{\odot} \text{ yr}^{-1} & \text{otherwise.} \end{cases} \quad (\text{A2})$$

This produces the jump-and-hook trajectory seen in Fig. A1 whose details are discussed in Section 3.1.

Due to the associated observational uncertainties, it is not immediately obvious from this figure whether any of these galaxies experienced a starburst accurately described by this model. A more detailed investigation would compare model predictions of stellar abundance and age distributions to the observed data, quantifying the relative likelihoods of various models with and without starbursts to constrain their evolutionary histories.

This paper has been typeset from a $\text{\TeX}/\text{\LaTeX}$ file prepared by the author.